# ABSTRACT


Title of Dissertation: Strongly correlated excitons in moiré semiconductors

Tsung-Sheng Huang
Doctor of Philosophy, 2025

Dissertation Directed by: Professor Mohammad Hafezi
Department of Physics
Department of Electrical and Computer Engineering
Joint Quantum Institute
Joint Center for Quantum Information and Computer Science



Moiré transition metal dichalcogenide (TMD) bilayers have emerged as a versatile platform for exploring a wide range of correlated electronic phenomena. In optical studies of these semiconducting systems, excitons—bound electron-hole pairs—play a crucial role by linking electronic correlations to optical responses. This thesis develops theoretical frameworks to understand how excitonic behavior interplays with various correlated states in moiré TMD bilayers and the resulting implications for optical measurements.

We begin by investigating the interaction between a single moiré exciton and Wigner crystal states formed by doped electrons. Focusing on systems with repulsive electron–exciton interactions, we discuss a scenario where excitons move within the complementary lattice of the charge-ordered electrons. As different Wigner crystal configurations emerge at specific

electron filling fractions, the effective exciton lattice changes accordingly, giving rise to distinct spectral and topological features. These characteristics can serve as optical signatures of the underlying charge order, and we propose a momentum- and polarization-resolved reflection experiment to detect them.

Next, we turn to undoped bilayers hosting multiple moiré excitons. While prior work often models these systems using a Bose-Hubbard framework, we show that their commutation relations deviate from those of conventional bosons. Instead, the excitons obey algebra similar to that of angular momentum operators, resulting in a finite Hilbert space and limiting local exciton occupancy to two or three, depending on the bilayer's specific parameters. We demonstrate that this occupancy constraint could manifest in high-intensity optical pumping experiments.

Finally, we explore exciton dynamics in a doped heterobilayer where the topmost valence moiré band forms an antiferromagnetic Mott insulator. We present a theoretical model describing the coupling between the exciton and the spin background, revealing that spin fluctuations substantially narrow the exciton's effective bandwidth—by orders of magnitude compared to its non-interacting counterpart. This suppression in mobility provides a measurable contrast, which we suggest can be probed through exciton diffusion experiments.

# Strongly correlated excitons in moiré semiconductors

by

Tsung-Sheng Huang

Dissertation submitted to the Faculty of the Graduate School of the
University of Maryland, College Park in partial fulfillment
of the requirements for the degree of
Doctor of Philosophy
2025

Advisory Committee:
Professor Mohammad Hafezi, Chair/Advisor
Professor Jay Deep Sau
Professor You Zhou
Professor Aaron Sternbach
Professor Ian B. Spielman
Professor Christopher Jarzynski

# Acknowledgments

I would like to express my deepest gratitude to my advisor, Professor Mohammad Hafezi, for his unwavering guidance, support, and mentorship throughout my research journey. His insights and encouragement have been invaluable to my academic and personal growth.

I am also profoundly thankful to my collaborators, including Professors Atac Imamoglu, Christopher Baldwin, Darrick Chang, Fengcheng Wu, Michael Knap, Victor Galitski, and You Zhou; postdoctoral theorists Andrey Grankin, Ming Xie, Peter Lunts, Yan-Qi Wang, Yang-Zhi Chou, and Yu-Xin Wang; postdoctoral experimentalists Daniel G. Suárez-Forero, Deric Session, and Mahmoud Jalali Mehrabad; and my colleagues Beini Gao, Pranshoo Upadhyay, and Supratik Sarkar.

I am grateful to the members of the Hafezi Group at the Joint Quantum Institute for fostering a collaborative and stimulating environment. In particular, I thank Alexander Schuckert, Apurva Padhye, Benyamin Remez, Christopher Flower, Eleanor Crane, En Jui Kuo, Ghadah Alshalan, Gautam Nambiar, Hossein Dehghani, Lida Xu, Mahdi Ghafariasl, Masoud Mohammadi-Arzanagh, Mathias Van Regemortel, Yijia Xu, Yu-An Chen, and Ze-Pei Cian.

I would also like to acknowledge Ajit Srivastava, Ana Asenjo-Garcia, Annabelle Bohrdt, and Fabian Grusdt for engaging and insightful discussions that contributed to my broader understanding of the field.

Finally, I would like to express my heartfelt gratitude to my parents, Chung-Hua Wang and Fang-bin Huang, for their unconditional love, support, and encouragement throughout this journey.

# Table of Contents

# List of Tables

# List of Figures

# Citation to previous works

This thesis is based on the following published works and preprints by the author:

- The contents follow mainly the review article: **Tsung-Sheng Huang** and Mohammad Hafezi. "Strongly correlated excitons in moiré semiconductors". In preparation for publication in AAMOP: Advances in Atomic, Molecular, and Optical Physics, Volume 74.

- Chapter 3: **Tsung-Sheng Huang**, Yu-Xin Wang, Yan-Qi Wang, Darrick Chang, Mohammad Hafezi, and Andrey Grankin. "Collective optical properties of moiré excitons". arXiv:2407.19611. Cited as Ref. [1].

- Chapter 4: **Tsung-Sheng Huang**, Peter Lunts, and Mohammad Hafezi. "Non-bosonic moiré excitons". Physical Review Letters 132.18 (2024): 186202. Cited as Ref. [2].

- Chapter 5: **Tsung-Sheng Huang**, Yang-Zhi Chou, Christopher L. Baldwin, Fengcheng Wu, and Mohammad Hafezi. "Mott-moiré excitons". Physical Review B 107.19 (2023): 195151. Cited as Ref. [3].

In addition, the thesis is relevant to the following works:

- **Tsung-Sheng Huang**, Christopher L. Baldwin, Mohammad Hafezi, and Victor Galitski. "Spin-mediated Mott excitons". Physical Review B 107.7 (2023): 075111. Cited as Ref. [4].

- Beini Gao, Daniel G. Suárez-Forero, Supratik Sarkar, **Tsung-Sheng Huang**, et al. "Excitonic Mott insulator in a Bose-Fermi-Hubbard system of moiré $WS_2/WSe_2$ heterobilayer." Nature Communications 15, 2305 (2024). Cited as Ref. [5].

- Pranshoo Upadhyay, Daniel G. Suárez-Forero, **Tsung-Sheng Huang**, et al. "Giant enhancement of exciton diffusion near an electronic Mott insulator." arXiv:2409.18357 (2024). Cited as Ref. [6].

- Beini Gao, Mahdi Ghafariasl, Mahmoud Jalali Mehrabad, **Tsung-Sheng Huang**, et al. "Probing Quantum Anomalous Hall States in Twisted Bilayer $WSe_2$ via Attractive Polaron Spectroscopy." In preparation.

- **Tsung-Sheng Huang**, Andrey Grankin, Yu-Xin Wang, and Mohammad Hafezi. "Optical engineering and detection of magnetism in moiré semiconductors". In preparation.

# Chapter 1: Introduction

The interplay between strongly correlated electron physics and photonics has recently attracted significant attention, as it broadens the scope of quantum sciences and technologies by providing a new direction to optically prepare, probe and manipulate hybrid photon-electron states [7, 8, 9, 10, 11].

Remarkably, experiments have utilized this interplay to optically engineer many-body correlations such as magnetism [12, 13] and superconductivity [14, 15, 16]. In turn, engineering optical properties, a central focus of quantum photonics and optoelectronics, may be achieved by accessing certain correlations in matter [17, 18, 19]. However, the origin of such effects and a microscopic understanding of such phenomena have remained elusive.

Recently, moiré semiconductors, particularly transition metal dichalcogenide (TMD) bilayers, have gained widespread interest as a promising platform for realizing strongly correlated electron-photon systems [20, 21, 22, 23]. On the optical side, these bilayers exhibit bandgaps in the visible and infrared frequency range [24], enabling efficient optical coupling to electronic interband transitions. Furthermore, the valley pseudospins in these materials can be tailored so that each couples predominantly to light with a different polarization [25], offering additional control over this degree of freedom. On the electronic side, the enlarged spatial periodicity of these superlattices suppresses charge kinetic energy [26], which, com-

bined with the typically weak dielectric screening in these materials [27], enhances the interaction-to-kinetic energy ratio, favoring strong electronic correlations. Various correlated electronic states have been theoretically investigated and experimentally observed in these bilayers, including Wigner crystals [28, 29], Mott insulators [26, 30], Kondo insulators [31, 32, 33], superconductivity [34, 35, 36, 37, 38, 39], and topologically nontrivial phases such as fractional Chern insulators [40, 41, 42, 43, 44]. Nevertheless, the study of their interplay with light, especially in the quantum regime, remains a largely open research avenue.

This motivates the study of excitons (electron-hole bound states [45]) and their charged counterparts, such as trions and exciton-polarons, in moiré bilayers, as these quasiparticles could play a role in linking electronic and optical properties. Specifically, light can generate these composite particles, and, conversely, they can influence optical responses [21], with their constituent charges naturally inheriting the electronic correlations present in the bilayers. As a result, excitons may serve as an optical probe of these correlated states. One example is the observed abrupt increase in excitonic energy when the doping level reaches one charge per moiré unit cell [46, 47, 5], an effect attributed to exciton-electron repulsion and often considered an indicator of the Mott insulating phase. Further insights into correlated electronic states could be gained by examining other excitonic properties, such as lifetime [48], valley contrast (circular dichroism) [49], and diffusion constants [6], as well as their dependence on factors like temperature and external magnetic field [49, 5, 6].

In addition to the above applications, which are primarily captured within the framework of single-exciton physics, intriguing many-body phenomena involving these excita-

tions can also emerge in these superlattices. For instance, moiré excitons have been shown to exhibit superfluidity [50, 51], a property that could potentially be useful for developing polariton lasers [52]. Another example is the emergence of correlated insulating excitonic states, which have (previously) been considered a realization of the Bose-Hubbard model [53, 47, 5]. The scope of simulating many-body Hamiltonians could be further extended to Bose-Fermi mixtures when doped charges are introduced to coexist with excitons in these moiré systems [47, 5, 54].

Despite the above experimental results, the theoretical understanding of how excitonic properties relate to strong correlations — both excitonic and electronic — remains an active area of research. In this article, we review several recent studies in this context. We begin in Section 2 with an overview of TMD properties, followed by discussions on the interplay between moiré excitons and various forms of electronic correlations. Section 3 summarizes how collective excitonic properties are influenced by different Wigner crystal states of doped electrons, based on Ref. [1]. In Section 4, we review the role of nonbosonic statistics in moiré excitons, which could significantly alter the conventional Bose-Hubbard description, as discussed in Ref. [2]. Section 5 explores the impact of spin order and fluctuations in doped electrons on exciton dynamics, following Ref. [3]. Finally, in Section 6, we summarize our findings and outline several potential directions for future studies on strongly correlated moiré excitons.

# Chapter 2: Summary on properties of transition metal dichalcogenides

We begin by reviewing the properties of TMD monolayers, which have the chemical formula $MX_2$, where $M \in Mo, W$ and $X \in S, Se, Te$ represent the metal and chalcogen atoms, respectively [55]. The lattice structure of these materials is shown in Fig. 2.1(a) and (b). In these monolayers, the atoms are arranged in an X–M–X configuration along the out-of-plane direction, with each atomic layer forming a triangular lattice. When viewed from the top, a monolayer TMD appears as a hexagonal lattice, with different atoms occupying distinct sublattices within the triangular unit cell.

*Band structures.* — In momentum space, the absence of sublattice symmetry (unlike in graphene) results in a gap between the lowest conduction band (CB) and the highest valence band (VB). The size of this bandgap, $\sim$ 1eV [24], classifies undoped TMDs as semiconductors and is typically the largest relevant energy scale in these systems. The CB

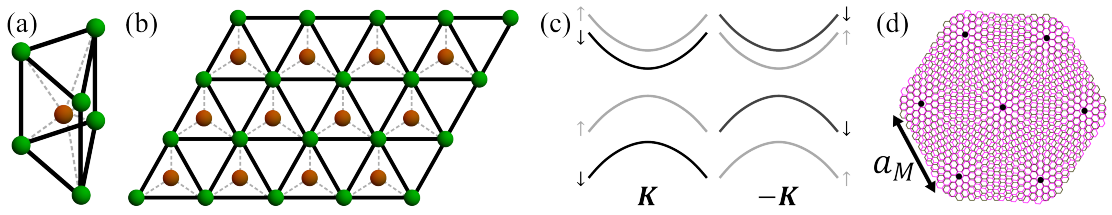


Figure 2.1: Properties of transition metal dichalcogenides (TMDs). (a) Unit cell of a TMD monolayer. (b) Top-view lattice structure, where green and orange dots represent chalcogen and transition metal atoms, respectively. (c) Schematic band diagram of a monolayer (illustrated for $WSe_2$ [26]), showing spin ($\uparrow$, $\downarrow$) and valley ($\pm\boldsymbol{K}$) degrees of freedom. (d) Moiré superlattice formed by stacking two TMD layers, with an enlarged periodicity $a_M$.

minimum and VB maximum are located at the corners of the hexagonal Brillouin zone (BZ) [24]. Note that up to a translation by reciprocal lattice vectors, there are only two inequivalent corner momenta, denoted as $\tau \boldsymbol{K}$ with $\tau \in \pm$, which define the *valleys*. At these high-symmetry points, the Bloch wavefunctions of the CB and VB primarily exhibit $|d_{z^2}\rangle$ and $|d_{x^2-y^2}\rangle + i\tau|d_{xy}\rangle$ orbital character, respectively [55]. As a result, electronic states with momenta near the valleys can be effectively described by a massive Dirac fermion model.

*Spin-valley locking.*— In addition to the Dirac term, TMDs exhibit significant spin-orbit coupling, with a magnitude of $\sim$ 10meV in the CB and $\sim$ 100meV in the VB [56]. Due to time-reversal symmetry, if a Bloch state is labeled by valley index $\tau$ and real spin $\sigma$, there must be a degenerate counterpart at $(-\tau, -\sigma)$. As a result, at low energies, the real-spin index can effectively be treated as locked to the valley degree of freedom and omitted from the description. Figure 2.1(c) illustrates the schematic band structure, incorporating these valley and spin features.

*Valley-polarization selectivity.*— Besides spin-valley locking, the valley degree of freedom is also subject to constraints in light-matter coupling. Specifically, optical transitions between CB and VB at valley $\tau$ only couple to circularly polarized light with polarization $\boldsymbol{e}_\tau = \frac{1}{\sqrt{2}}(\boldsymbol{e}_x + i\tau \boldsymbol{e}_y)$, where $\boldsymbol{e}_x$ and $\boldsymbol{e}_y$ are Cartesian in-plane unit vectors [25]. This valley-selective coupling arises from (a) the threefold rotational ($\hat{C}_3$) symmetry of the underlying lattice, and (b) the fact that the valley momenta $\tau \boldsymbol{K}$ are equivalent under $\hat{C}_3$ rotation. As a result, the Bloch states at these high-symmetry points — denoted $|\Psi^c_{\tau \boldsymbol{K}}\rangle$ and $|\Psi^v_{\tau \boldsymbol{K}}\rangle$ for the CB and VB, respectively — form representations of the $\hat{C}_3$ rotation. More concretely, since (as mentioned earlier) $|\Psi^c_{\tau \boldsymbol{K}}\rangle \sim |d_{z^2}\rangle$ and $|\Psi^v_{\tau \boldsymbol{K}}\rangle \sim |d_{x^2-y^2}\rangle + i\tau|d_{xy}\rangle$ [55],

these states transform under $\hat{C}_3$ as $\hat{C}_3|\Psi^c_{\pm\boldsymbol{K}}\rangle = |\Psi^c_{\pm\boldsymbol{K}}\rangle$ and $\hat{C}_3|\Psi^v_{\pm\boldsymbol{K}}\rangle = e^{\pm i\frac{4\pi}{3}}|\Psi^v_{\pm\boldsymbol{K}}\rangle$, corresponding to angular momenta 0 and $\pm 2$, respectively. Following Wigner-Eckart theorem, and noting that angular momentum is defined modulo 3 under $\hat{C}_3$ lattice symmetry — so that $\pm 2 \equiv \mp 1$ — the optical transition matrix element between $|\Psi^c_{\tau\boldsymbol{K}}\rangle$ and $|\Psi^v_{\tau\boldsymbol{K}}\rangle$ must align with $\boldsymbol{e}^*_\tau$. Therefore, transitions at valley $\tau$ couple only to electric fields polarized along $\boldsymbol{e}_\tau$. Notably, this selection rule is strictly valid only for monolayers, as interlayer coupling in bilayers can modify the symmetries of electronic wavefunctions. Nevertheless, if the exciton is concentrated around certain high-symmetry points of the moiré landscape, this selectivity persist to some extent [57], which we assume to be the case in the following.

## 2.1 Moiré bilayers

Stacking two TMD monolayers with a twisting angle $\theta$ or a lattice mismatch results in a bilayer with an enlarged periodicity of $a_M \sim 10$ nm [2], significantly larger than the monolayer lattice constant of $\simeq 0.3$ nm [24], as illustrated in Fig.2.1(d). The charge dynamics in such a system is influenced by a superpotential arising from interlayer coupling, whose local extrema form a triangular or hexagonal superlattice[26, 58]. As a result, the monolayer band structures fold into a hexagonal moiré Brillouin zone (mBZ) and split into moiré bands. The bandwidths of these minibands and the energy gaps between them depend on $a_M$ as well as the specific material composition. For experimentally accessible samples, the characteristic energy scales of the lowest conduction and highest valence moiré bands (denoted as CMB and VMB, respectively) typically range from $\sim 1$ to $\sim 10$ meV [59, 60]. Fitting these bands to tight-binding models suggests that the corresponding

nearest-neighbor hopping amplitudes are on the order of $\sim 0.1$ to $\sim 1$ meV [1].

*Strong correlations.* — In contrast, electron-electron interactions in moiré systems can be as large as $\sim 100$ meV [26], indicating the presence of strong correlations. In moiré heterobilayers, interacting electrons can be described by a generalized Hubbard model that incorporates on- and off-site Coulomb interactions [26, 28]. This framework accounts for the emergence of charge-ordered states, such as Mott insulators and Wigner crystals, along with the associated spin correlations. For homobilayers, however, the description differs due to the presence of layer degeneracies, which can give rise to nontrivial band topology. More complicated models, such as the Kane-Mele model [58] and the SU(4)-generalized Hubbard model [61], have been proposed to describe the interplay between topology and strong correlations.

*Moiré excitons.* — Another important degree of freedom in moiré TMD bilayers is excitons — bound states formed by a conduction band electron and a valence band hole. As mentioned earlier, these excitations serve as a bridge between underlying electronic correlations and optical responses [20, 21, 22, 23]. These quasiparticles can be categorized as *intralayer* or *interlayer* excitons [62, 25], depending on whether the electron and hole reside in the same layer — though, strictly speaking, they can hybridize [63]. Interlayer excitons generally possess a permanent dipole moment oriented along the out-of-plane direction [64, 2], whereas intralayer excitons do not. As a result, interlayer excitons typically experience stronger on-site repulsion compared to their intralayer counterparts. However, interlayer excitons also exhibit a smaller transition dipole moment due to the spatial separation between the electron and hole, as well as the effects of twisting or lattice mis-

[1] Note that for a triangular lattice, the hopping integral and bandwidth differ by a factor of 9.

match, which reduce wavefunction overlap [65, 66]. Consequently, intralayer excitons tend to produce a stronger optical response in reflection measurements compared to interlayer excitons [67]. Notably, the relative energy of intralayer and interlayer excitons depends on the band alignment between the two layers. In the remainder of this article, we focus specifically on type-II band alignment, where the CB minimum and VB maximum of one TMD layer are lower than those of the other layer [25]. In this scenario, interlayer excitons typically have lower energy than intralayer excitons and thus dominate photoluminescence measurements [67].

## 2.2 Mathematical description of the electron-photon system

We proceed to outline the mathematical description of strongly correlated moiré excitons. As a starting point, we consider the electron-photon parent Hamiltonian $\hat{\mathcal{H}} = \hat{\mathcal{H}}_0 + \hat{\mathcal{H}}_L + \hat{\mathcal{H}}_T$. Here, $\hat{\mathcal{H}}_0$ includes the kinetic energy and atomic potentials of the electronic degrees of freedom. For simplicity, we focus on the low-energy dynamics, considering only the CB and VB within the lowest spin-valley sector. Furthermore, we specifically consider heterobilayers, where the interlayer coupling is perturbative compared to the layer band offsets [24, 68], and therefore, the primary effect of this coupling is to yield a moiré potential (rather than induce layer hybridization [58]). These considerations lead to:

$$\hat{\mathcal{H}}_0 = \sum_{n=c,v} \sum_{\tau} \int d^2\boldsymbol{s}\, \hat{\psi}_{\tau}^{(n)\dagger}(\boldsymbol{s}) h_n(\boldsymbol{s}) \hat{\psi}_{\tau}^{(n)}(\boldsymbol{s}), \quad h_n(\boldsymbol{s}) = \frac{\hat{\boldsymbol{p}}_{n,\tau}^2}{2m_n} + \Delta_n(\boldsymbol{s}) + (\delta_{n,c} - \delta_{n,v})(E_n^0 + \mu), \tag{2.1}$$

where $\boldsymbol{s}$ denotes the in-plane coordinates, $\tau \in \pm$ labels the valleys, and $n \in c, v$ represents the band index. The operators $\hat{\psi}_\tau^{(c)}(\boldsymbol{s})$ and $\hat{\psi}_\tau^{(v)}(\boldsymbol{s})$ correspond to the annihilation operators for CB electrons and VB holes, respectively, with their effective masses given by $m_c$ and $m_v$. $\hat{\boldsymbol{p}}_{n,\tau}$ describes the momentum relative to the $\tau$-valley momentum for band $n$, $\Delta_n(\boldsymbol{s})$ represents the moiré potential, $E_n^0$ is the energy offset for the corresponding band, and $\mu$ denotes the chemical potential.

The charge degrees of freedom interact with electromagnetic fields. We adopt the Coulomb gauge, where the sector involving only the longitudinal electromagnetic field, $\hat{\mathcal{H}}_L$, ultimately reduces to a quartic interaction between charges. For simplicity, in the rest of this article, we focus on two specific components of this interaction, $\hat{\mathcal{H}}_L \simeq \hat{\mathcal{V}}_e + \hat{\mathcal{V}}_{d,L}$. Here, $\hat{\mathcal{V}}_e$ depends only on the density operator, defined as $\hat{\rho}^{(n)}(\boldsymbol{s}) = \sum_\tau \hat{\psi}_\tau^{(n)\dagger}(\boldsymbol{s})\hat{\psi}_\tau^{(n)}(\boldsymbol{s})$, while $\hat{\mathcal{V}}_{d,L}$ depends only on the electric polarization operator, given by $\hat{\boldsymbol{P}}^\dagger(\boldsymbol{s}) = \sum_\tau \boldsymbol{d}_\tau^{cv} \hat{c}_\tau^\dagger(\boldsymbol{s})\hat{v}_\tau^\dagger(\boldsymbol{s})$, with $\boldsymbol{d}_\tau^{cv} = d\boldsymbol{e}_\tau^*$ representing the transition dipole moment from the VB to the CB at valley $\tau$. These components have the following expressions:

$$\hat{\mathcal{V}}_e = \frac{e^2}{8\pi\epsilon} \int d^2\boldsymbol{s} d^2\boldsymbol{s}' \frac{:\hat{\rho}_c(\boldsymbol{s})\hat{\rho}_c(\boldsymbol{s}'):}{|\boldsymbol{s}-\boldsymbol{s}'|} - \frac{2\hat{\rho}_c(\boldsymbol{s})\hat{\rho}_v(\boldsymbol{s}')}{\sqrt{(\boldsymbol{s}-\boldsymbol{s}')^2+z^2}}, \tag{2.2}$$

$$\hat{\mathcal{V}}_{d,L} = \frac{1}{\epsilon_0} \int d^2\boldsymbol{s} d^2\boldsymbol{s}' \hat{\boldsymbol{P}}^\dagger(\boldsymbol{s}) \cdot \left[\nabla_{\boldsymbol{s}} \otimes \nabla_{\boldsymbol{s}'} \frac{1}{|\boldsymbol{s}-\boldsymbol{s}'|}\right] \cdot \hat{\boldsymbol{P}}(\boldsymbol{s}'). \tag{2.3}$$

where $-e$ represents the electron charge. The parameter $z$ denotes the vertical displacement between CMB electrons and VMB holes, which corresponds to the interlayer separation, or zero, depending on whether these charges are in different layers or the same layer, respectively. The colons indicate that the operators between them are normal-ordered.

Note that we assume static dielectric screening but no dynamic screening, such that $\hat{\mathcal{V}}_e$ and $\hat{\mathcal{V}}_{d,L}$ are assigned the electric permittivity of the material and vacuum, respectively.

On the other hand, $\hat{\mathcal{H}}_T$ describes the sector that includes transverse electromagnetic fields and is given by the following expression:

$$\hat{\mathcal{H}}_T \simeq -\int d^2\boldsymbol{s}\left[\hat{\boldsymbol{P}}^\dagger(\boldsymbol{s})\cdot\hat{\boldsymbol{E}}_T(\boldsymbol{s})+\text{H.c.}\right]+\frac{\epsilon_0}{2}\int d^3\boldsymbol{r}\hat{\boldsymbol{E}}_T^\dagger(\boldsymbol{r})\hat{\boldsymbol{E}}_T(\boldsymbol{r})+c^2\hat{\boldsymbol{B}}^\dagger(\boldsymbol{r})\hat{\boldsymbol{B}}(\boldsymbol{r}), \quad (2.4)$$

where $\boldsymbol{r}$ represents the coordinates in three-dimensional space. The constant $c$ denotes the speed of light, and $\hat{\boldsymbol{E}}_T(\boldsymbol{r})$ and $\hat{\boldsymbol{B}}(\boldsymbol{r})$ are the transverse electric and magnetic field operators, respectively. Assuming that the relevant photon fluctuations have frequencies near the target exciton state, $\omega_{\text{ex}}$, one can integrate out these fluctuations, leading to the transformation of $\hat{\mathcal{H}}_T$ into $\hat{\mathcal{V}}_{d,T}$. Since $\hat{\mathcal{V}}_{d,T}$ depends only on the electric polarization, it can be combined with $\hat{\mathcal{V}}_{d,L}$ to yield:

$$\hat{\mathcal{V}}_d \equiv \hat{\mathcal{V}}_{d,L}+\hat{\mathcal{V}}_{d,T}=\frac{\omega_{\text{ex}}^2}{c^2\epsilon_0}\int d^2\boldsymbol{s}d^2\boldsymbol{s}'\hat{\boldsymbol{P}}^\dagger(\boldsymbol{s})\cdot\boldsymbol{\mathcal{G}}\left(\omega_{\text{ex}},\boldsymbol{s}-\boldsymbol{s}'\right)\cdot\hat{\boldsymbol{P}}(\boldsymbol{s}'), \quad (2.5)$$

where $\mathcal{G}_{\alpha,\beta}(ck,\boldsymbol{r})$ denotes the ($\alpha,\beta\in x,y,z$ components of) dyadic Green's tensor:

$$\mathcal{G}_{\alpha,\beta}(ck,\boldsymbol{r})=-\frac{e^{ikr}}{4\pi r}\left[\left(1+\frac{i}{kr}-\frac{1}{(kr)^2}\right)\delta_{\alpha,\beta}+\left(-1-\frac{3i}{kr}+\frac{3}{(kr)^2}\right)\frac{r_\alpha r_\beta}{r^2}\right]+\frac{\delta_{\alpha,\beta}\delta^{(3)}(\boldsymbol{r})}{3k^2}. \quad (2.6)$$

In summary, we have transformed the electron-photon parent Hamiltonian into $\hat{\mathcal{H}}\simeq\hat{\mathcal{H}}_0+\hat{\mathcal{V}}_e+\hat{\mathcal{V}}_d$. In the following, we discuss how to further simplify this model to describe the physics of strongly correlated electrons and a single exciton, respectively. These simplified

models, as well as other effective models derived from $\hat{\mathcal{H}}$ to study the physics in various regimes, are summarized in Table. 2.1.

| $n_{\text{ex}}$ \ $\lvert\nu_e\rvert$ | 0 (undoped) | $\frac{1}{4}, \frac{1}{3}, \frac{1}{2}, \frac{2}{3}, \frac{3}{4}, \frac{6}{7}$ (WCs) | 1 (Mott insulator) |
|---|---|---|---|
| 0 | (Trivial) | Generalized Hubbard model: Eq. (2.7) | Generalized Hubbard model: Eq. (2.7) |
| 1 | Electron-hole binding in moiré potential: . Eq. (2.8) | Exciton dynamics driven by dipolar interaction restricted by WCs: Eq. (3.1) in Sec. 3. | Exciton dynamics dressed by fluctuations on top of spin order: Eq. (5.1) in Sec. 5. |
| $\geq 2$ | Interacting model of nonbosonic excitons: Eq. (4.6) in Sec. 4. | | |

Table 2.1: Effective models and the topic discussed at various charge filling fractions $|\nu_e|$ and exciton number in the system $n_{\text{ex}}$.

### 2.2.1 Effective model: zero-exciton subspace with doped charges

We first review the strong correlations of doped charges in moiré TMDs. For simplicity, in this section, we focus on the case where excess charges (CMB electrons and VMB holes) occupy a single moiré band, leaving the discussion of exciton incorporation to a later section. Under these conditions, $\hat{\mathcal{H}}$ can be projected onto the subspace spanned by CMB electrons and VMB holes. Denoting their annihilation operators as $\hat{c}_{\boldsymbol{R},\tau}$ and $\hat{v}_{\boldsymbol{R},\tau}$, respectively, $\hat{\mathcal{H}}$ reduces to $\hat{H}_c + \hat{H}_v$, where:

$$\hat{H}_c = E_c \sum_{\boldsymbol{R},\tau} \hat{c}^\dagger_{\boldsymbol{R},\tau}\hat{c}_{\boldsymbol{R},\tau} - \sum_{\tau}\sum_{\boldsymbol{R},\boldsymbol{R}'} t^c_{\boldsymbol{R}',\boldsymbol{R}}\hat{c}^\dagger_{\boldsymbol{R}',\tau}\hat{c}_{\boldsymbol{R},\tau} + \frac{1}{2}\sum_{\tau,\tau'}\sum_{\boldsymbol{R},\boldsymbol{R}'} U_c(\boldsymbol{R}-\boldsymbol{R}')\hat{c}^\dagger_{\boldsymbol{R},\tau}\hat{c}^\dagger_{\boldsymbol{R}',\tau'}\hat{c}_{\boldsymbol{R}',\tau'}\hat{c}_{\boldsymbol{R},\tau}. \tag{2.7}$$

Here, $E_c$ and $t^c_{\boldsymbol{R}',\boldsymbol{R}}$ represent the occupation energy and hopping integrals of CMB electrons, respectively, which correspond to the matrix elements of $h_c(\boldsymbol{s})$ in the basis of their moiré-

Wannier orbitals. The term $U_c(\boldsymbol{R}-\boldsymbol{R}')$ denotes the repulsion between CMB electrons arising from $\hat{\mathcal{V}}_e$. The expression for $\hat{H}_v$ follows similarly, with the replacements $\hat{c}_{\boldsymbol{R},\tau} \to \hat{v}_{\boldsymbol{R},\tau}$, $E_c \to E_v$, $t^c_{\boldsymbol{R}',\boldsymbol{R}} \to t^v_{\boldsymbol{R}',\boldsymbol{R}}$, and $U_c(\boldsymbol{R}-\boldsymbol{R}') \to U_v(\boldsymbol{R}-\boldsymbol{R}')$. The generalized Hubbard models $\hat{H}_c$ and $\hat{H}_v$ have been theoretically demonstrated to give rise to correlated states such as Wigner crystals and Mott insulators in moiré TMD bilayers [26, 28].

### 2.2.2 Effective model: single-exciton subspace without doped charges

Next, we discuss how to incorporate excitonic degrees of freedom into the model, beginning with the case of a single exciton in the absence of excess charges. In general, a single moiré exciton in a TMD bilayer can be described by the two-body Schrödinger equation governed by $\hat{\mathcal{H}}$. For simplicity, we initially neglect $\hat{\mathcal{V}}_d$ and will discuss its role later. This leads to the following equation (with $\hbar = 1$ set throughout this article):

$$\left[-\frac{\nabla^2_{\boldsymbol{s}_c}}{2m_c} + \Delta_c(\boldsymbol{s}_c) - \frac{\nabla^2_{\boldsymbol{s}_v}}{2m_v} + \Delta_v(\boldsymbol{s}_v) - \frac{e^2}{\epsilon\sqrt{(\boldsymbol{s}_c-\boldsymbol{s}_v)^2+z^2}} - E_{l,\boldsymbol{Q}}\right]\phi_{l,\boldsymbol{Q}}(\boldsymbol{s}_c,\boldsymbol{s}_v) \simeq 0, \quad (2.8)$$

where $\boldsymbol{s}_c$ and $\boldsymbol{s}v$ denote the in-plane positions of the electron and hole, respectively. The parameters $m_c$ and $m_v$ represent the masses of a CB electron and a VB hole, respectively. The moiré potentials $\Delta_c(\boldsymbol{r})$ and $\Delta_v(\boldsymbol{r})$ exhibit a spatial periodicity of $a_M$. The index $l \in 0, 1, 2, \ldots$ labels all internal states, including excitonic moiré bands and levels associated with relative motion. The total superlattice momentum is given by $\boldsymbol{Q}$, and $\phi_{l,\boldsymbol{Q}}(\boldsymbol{s}_c,\boldsymbol{s}_v)$ represents the corresponding exciton Bloch wavefunction (with the valley index suppressed for simplicity), associated with the energy $E_{l,\boldsymbol{Q}}$.

Solutions to Eq. (2.8) can be analytically derived in two perturbative regimes, re-

ferred to as the *strong Coulomb regime* and the *deep moiré limit*. In the strong Coulomb regime, the electron-hole Coulomb attraction dominates over the moiré potentials in determining the relative dynamics. Consequently, $\phi_{l,\boldsymbol{Q}}(\boldsymbol{s}_c, \boldsymbol{s}_v)$ is approximately a product of two functions, one depending only on $\boldsymbol{s}_x = \frac{m_c}{M}\boldsymbol{s}_c + \frac{m_v}{M}\boldsymbol{s}_v$ ($M = m_c + m_v$) and the other on $\boldsymbol{s}_l = \boldsymbol{s}_c - \boldsymbol{s}_v$. In contrast, in the deep moiré limit, the Coulomb attraction acts as a perturbation, so $\phi_{l,\boldsymbol{Q}}(\boldsymbol{s}_c, \boldsymbol{s}_v)$ is nearly a product state of a CB electron and a VB hole. However, in this case, capturing electron-hole correlation requires incorporating at least the first-order perturbation.

By applying a Fourier transform to these moiré-Bloch wavefunctions, one can obtain the moiré-Wannier functions of excitons centered at a moiré site $\boldsymbol{R}$, denoted as $W_{l,\boldsymbol{R}}(\boldsymbol{s}_c, \boldsymbol{s}_v) = \frac{1}{\sqrt{N}}\sum_{\boldsymbol{Q}} e^{-i\boldsymbol{Q}\cdot\boldsymbol{R}}\phi_{l,\boldsymbol{Q}}(\boldsymbol{s}_c, \boldsymbol{s}_v)$ with $N = \sum_{\boldsymbol{R}} 1$. For the remainder of this article, we will focus solely on the lowest excitonic orbital $w_{\boldsymbol{R}}(\boldsymbol{s}_c, \boldsymbol{s}_v) \equiv W_{0,\boldsymbol{R}}(\boldsymbol{s}_c, \boldsymbol{s}_v)$ unless otherwise noted. The corresponding exciton annihilation operator is then:

$$\hat{x}^\dagger_{\boldsymbol{R},\tau} = \int d^2\boldsymbol{s}_c d^2\boldsymbol{s}_v w_{\boldsymbol{R}}(\boldsymbol{s}_c, \boldsymbol{s}_v)\hat{\psi}^{(c)\dagger}_\tau(\boldsymbol{s}_c)\hat{\psi}^{(v)\dagger}_\tau(\boldsymbol{s}_v), \tag{2.9}$$

where we consider R-stacked bilayers throughout the article, such that the two charges have the same $\tau$ [69]. Note that in the deep moiré limit, $w_{\boldsymbol{R}}(\boldsymbol{s}_c, \boldsymbol{s}_v)$ becomes the product of the wavefunctions of the CMB electron and VMB hole. Therefore, $\hat{x}^\dagger_{\boldsymbol{R},\tau} \simeq \hat{c}^\dagger_{\boldsymbol{R},\tau}\hat{v}^\dagger_{\boldsymbol{R},\tau}$.

One can, in turn, determine whether an exciton wavefunction is in the strong Coulomb regime or the deep moiré limit by comparing the following two scales:

$$(a^x_W)^2 \equiv \int d\boldsymbol{s}_c d\boldsymbol{s}_v |w_{\boldsymbol{R}}(\boldsymbol{s}_c, \boldsymbol{s}_v)|^2(\boldsymbol{s}_x - \boldsymbol{R})^2, \quad \langle s_l^2\rangle \equiv \int d\boldsymbol{s}_c d\boldsymbol{s}_v |w_{\boldsymbol{R}}(\boldsymbol{s}_c, \boldsymbol{s}_v)|^2 s_l^2. \tag{2.10}$$

In the strong Coulomb regime, $(a_W^x)^2 \gg \langle s_l^2 \rangle \sim a_B^2$, where $a_B = \frac{M\epsilon}{e^2 m_c m_v}$ is the Bohr radius. In contrast, in the deep moiré regime, one finds $(a_W^x)^2 \sim \langle s_l^2 \rangle \ll a_B^2$.

Finally, we discuss how $\hat{\mathcal{V}}_d$ modifies the single exciton properties. First, we note that it only contributes to the center-of-mass kinetic energy of the exciton and does not directly impact the relative dynamics, suggesting that the previous discussion regarding the two perturbative regimes still holds. Second, $\hat{\mathcal{V}}_d$ generically mixes the lowest and higher exciton levels; nevertheless, the lowest excitonic level is still roughly captured by $w_{\boldsymbol{R}}(\boldsymbol{s}_c, \boldsymbol{s}_v)$ if the strength of the transition dipole is weak compared to $ea_B$ and $ea_W^x$. This can be confirmed by evaluating the energy scales from the dynamics within a moiré unit cell. Specifically, given that $\omega_{\text{ex}} a_M / c \ll 1$, the energy given by $\hat{\mathcal{V}}_d$ scales as $\sim \frac{|d^2|}{\epsilon a_W^3}$ (recall that $|d|$ is the magnitude of the transition dipole), whereas the intrinsic charge motion gives $\sim \frac{1}{2Ma_W^2}$. Therefore, the profile of the exciton Wannier orbital near its center is not drastically modified if $a_W \gg \frac{|d|^2}{e^2 a_B}$ (assuming $m_c \sim m_v$), which is typically true for interlayer excitons. On the other hand, the tunneling between moiré sites due to intrinsic charge motion and from $\hat{\mathcal{V}}_d$ scales differently with distance. Specifically, the former scales exponentially, while the latter scales as a power law. Therefore, the comparison between them depends on the details of the system under consideration, and we leave the discussion of it to the following sections.

# Chapter 3: Moiré excitons coexisting with charge-ordered states of doped electrons

We proceed by reviewing the interplay between an exciton and the charge orders of doped electrons in moiré TMD heterobilayers, following Ref.3. The scenario is summarized as follows: When exciton-electron repulsion is included, the exciton can only hop between vacant supersites and cannot tunnel into a moiré unit cell where a doped charge is already located. See Fig.3.1(a). The charge orders thus act as additional superpotentials to the exciton, thereby influencing its collective optical properties. Furthermore, distinct Wigner crystal (WC) states can emerge at different charge filling fractions $\nu_e$ [see Fig.3.1(b)]. Since $\nu_e$ can be tuned by gate voltage, the corresponding collective excitonic properties can be readily accessed and serve as experimental signatures of the WCs. These properties are summarized in Table3.1.

## 3.1 Effective model: single-exciton subspace with charge-ordered doped electrons

As stated in Section 2, the CB and VB of an R-stacked heterobilayer are considered. The system of interest consists of doped electrons in the CB and a single exciton formed by

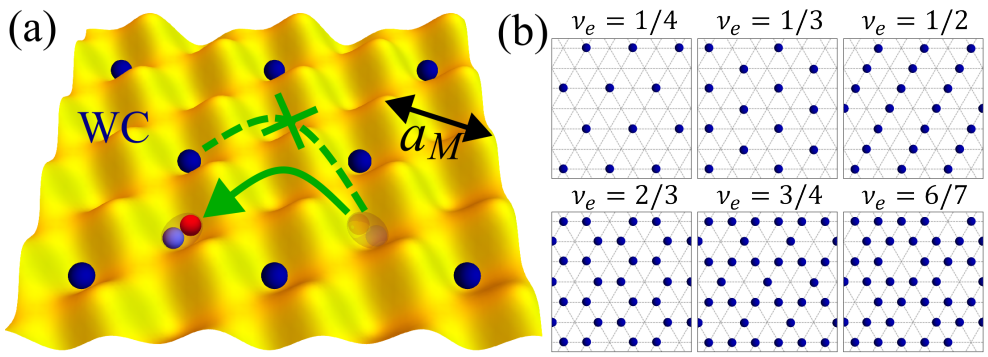


Figure 3.1: (a) Constrained exciton (pair of red and light blue dots) tunneling due to the presence of the charge order state of doped electrons (dark blue). The tunneling originates from the dipole-dipole interaction $\hat{\mathcal{V}}_d$ (green arrow), and therefore is long-ranged. Nevertheless, exciton-electron repulsion prevents the exciton from populating the sites that are already occupied by electrons. The yellow surface represents the moiré potential with period $a_M$. (b) Charge orders emerging at various $\nu_e$ in untwisted $WSe_2/WS_2$ [29, 70]. The remaining vacant sites provide an effective excitonic lattice as demonstrated in panel (a). Figure reproduced from Ref. [1].

charges in the two bands. For simplicity, all electrons (both doped and optically excited) are assumed to reside in the same layer. The moiré period $a_M$ is taken to be sufficiently large so that tunneling from intrinsic charge motion is suppressed compared to hopping driven by $\hat{\mathcal{V}}_d$ [1]. Together with the assumption that exciton-electron repulsion is significant compared to exciton tunneling, the low-energy (non-Hermitian) Hamiltonian is given by:

$$\hat{H} = \left(\omega_{\text{ex}} - \frac{i\gamma}{2}\right) \sum_{\tilde{\boldsymbol{R}},\tau} \hat{x}^\dagger_{\tilde{\boldsymbol{R}},\tau} \hat{x}_{\tilde{\boldsymbol{R}},\tau} + \frac{\omega_{\text{ex}}^2 |d|^2}{c^2 \epsilon_0} \sum_{\tilde{\boldsymbol{R}} \neq \tilde{\boldsymbol{R}}'} \sum_{\tau,\tau'} \boldsymbol{e}^*_\tau \cdot \boldsymbol{\mathcal{G}}^{\text{ex}}\left(\tilde{\boldsymbol{R}} - \tilde{\boldsymbol{R}}'\right) \cdot \boldsymbol{e}_{\tau'} \hat{x}^\dagger_{\tilde{\boldsymbol{R}},\tau} \hat{x}_{\tilde{\boldsymbol{R}}',\tau'}, \quad (3.1)$$

where $\omega_{\text{ex}}$ and $\gamma$ denote the bare exciton energy and decay rate, respectively. The function $\boldsymbol{\mathcal{G}}^{\text{ex}}(\boldsymbol{R} - \boldsymbol{R}')$ is defined as $\int_{\boldsymbol{s},\boldsymbol{s}'} w^*_{\boldsymbol{R}}(\boldsymbol{s},\boldsymbol{s}) \boldsymbol{\mathcal{G}}(\omega_{\text{ex}}; \boldsymbol{s} - \boldsymbol{s}') w_{\boldsymbol{R}'}(\boldsymbol{s}',\boldsymbol{s}')$, where the exciton Wannier orbitals are approximated using the perturbative solution of Eq.(2.8) in the strong Coulomb limit for simplicity. The sets $\{\tilde{\boldsymbol{R}}\}$ and $\{\tilde{\boldsymbol{R}}'\}$ correspond to moiré sites unoccupied

[1] This approximation is valid because exciton hopping from intrinsic charge motion decays exponentially with distance, whereas exciton tunneling driven by $\hat{\mathcal{V}}_d$ follows a power-law scaling.

| $\nu_e$ | Emergent arrays | Superradiant $\Lambda$ | $C_{\mathrm{LC}}$ |
|---|---|---|---|
| $0, \frac{2}{3}, \frac{3}{4}, \frac{6}{7}$ | Triangular | $0, 1$ | $-1, 1$ |
| $\frac{1}{2}$ | Rectangular | $0, 1$ | $0, 0$ |
| $\frac{1}{3}$ | Honeycomb | $0, 1$ | $-1, 1$ |
| $\frac{1}{4}$ | Kagome | $0, 1, 3, 4$ | $-1, 1, 1, -1$ |

Table 3.1: Properties of an interlayer exciton in electron-doped, untwisted $WSe_2/WS_2$. The first column lists electron filling fractions ($\nu_e$) that exhibit charge order [29, 70]. The second column shows the corresponding effective lattice for the exciton, which emerges as the complementary lattice to the charge order. The third column presents the collective band indices ($\Lambda$, ordered by energy), that exhibit enhanced radiative decay (within the light cone) compared to the bare dipole transition rate $\gamma$. The last column provides the total Berry curvature, $C_{\mathrm{LC}}$, summed over all momenta within the light cone. The calculation of $C_{\mathrm{LC}}$ includes an out-of-plane magnetic field introducing Zeeman splitting of $\mu_B B = 20\gamma$. Table reproduced from Ref. [1].

by doped charges. These excess charges, governed by Eq.(2.7), can form WCs at specific $\nu_e$ values. The charge order is assumed to remain stable against the motion of a single exciton, making $\{\tilde{\boldsymbol{R}}\}$ the complementary lattice to the WC at the corresponding fractional fillings.

## 3.2 Collective spectral properties of moiré excitons

The eigenvalues of Eq. (3.1) corresponding to the single-excitation states can be expressed as $\omega_{\mathrm{ex}} + \Delta_{\boldsymbol{Q}} - \frac{i}{2}\Gamma_{\boldsymbol{Q}}$, where $\Delta_{\boldsymbol{Q}}$ and $\Gamma_{\boldsymbol{Q}}$ are real values that characterize the collective lineshifts and linewidths of the exciton, respectively. The collective effects are generally significant, as the moiré superlattice is deep subwavelength ($\omega_{\mathrm{ex}} a_M / c \ll 1$). Specifically, $\Gamma_{\boldsymbol{Q}}/\gamma$ is expected to scale with the number of complementary lattice sites within the area of the exciton wavelength squared, assuming constructive interference of excitonic states

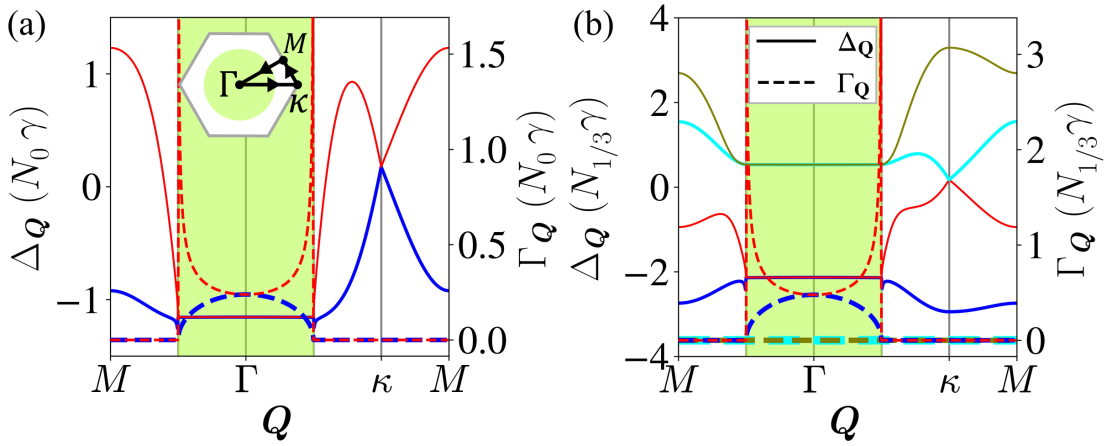


Figure 3.2: Collective excitonic bands in charge-ordered untwisted $WSe_2/WS_2$. Solid and dashed lines represent the excitonic lineshifts ($\Delta_{\boldsymbol{Q}}$) and linewidths ($\Gamma_{\boldsymbol{Q}}$), respectively, for electron fillings (a) $\nu_e = 0$ and (b) $\nu_e = \frac{1}{3}$. Curves of the same color correspond to the same excitonic band. The vertical axes are scaled by $\gamma N_{\nu_e}$, where $N_{\nu_e}$ is defined in Eq. (3.2) and is of order $\sim 10^4$ here. The horizontal axes represent Bloch momenta $\boldsymbol{Q}$ along a piecewise-linear path through high-symmetry points in the Brillouin zone, as illustrated by the hexagon in the inset of (a). Momenta within the light cone are highlighted by the green shaded region (enlarged for clarity). Figure reproduced from Ref. [1].

at all these sites. This number is defined for a $\nu_e$-doped bilayer with twisting angle $\theta$ as:

$$N_{\nu_e}(\theta) = (1 + \theta^2/\delta^2)N_{\nu_e}, \quad N_{\nu_e} = \lambda_{\text{ex}}^2/\mathcal{A}_{\nu_e}, \tag{3.2}$$

where $\mathcal{A}_{\nu_e}$ represents the unit cell area of the complementary lattice at zero twist and $\delta$ denotes the mismatch between the lattice spacings of the two TMD layers. Using this quantity, the degree of constructive interference can be estimated by evaluating $\frac{\Gamma_{\boldsymbol{Q}}}{\gamma N_{\nu_e}(\theta)}$.

Fig. 3.2 shows $\Delta_{\boldsymbol{Q}}$ and $\Gamma_{\boldsymbol{Q}}$ for triangular and honeycomb excitonic lattices from $\nu_e = 0$- and $\nu_e = 1/3$-doped $WSe_2/WS_2$ at zero twist, respectively. The collective bands from these $\nu_e$ values share several common properties. Within the lightcone (LC), the fact that $\Gamma_{\boldsymbol{Q}}$ scales with $N_{\nu_e}\gamma$ ($N_{\nu_e} \sim 10^4$ for the parameters used) indicates strong constructive interference. Such a large decay rate also suggests that an exciton tends to emit light

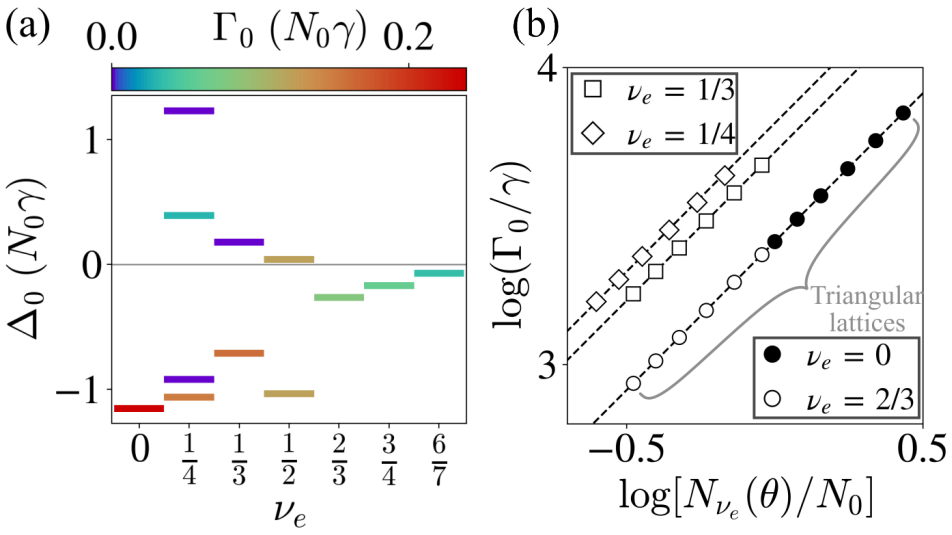


Figure 3.3: Optical signatures of charge orders at various electron fillings $\nu_e$. (a) Collective excitonic band properties at $\boldsymbol{Q} = 0$ for untwisted $WSe_2/WS_2$, and (b) their dependence on the twisting angle, which is captured in the combined factor $N_{\nu_e}(\theta)$ defined in Eq.(3.2). Dashed lines in (b) represent linear fits with a slope of 1. Figure reproduced from Ref.[1].

before tunneling to other moiré sites. This is consistent with the relatively flat dispersion $\Delta_{\boldsymbol{Q}}$ within the LC. In contrast, outside the LC, $\Gamma_{\boldsymbol{Q}}$ is suppressed, indicating destructive interference for those momenta. Qualitatively, this occurs because the exciton momentum is too large for the exciton-light momentum conservation to be satisfied.

On the other hand, there are other properties of the collective bands that vary with $\nu_e$, which could serve as experimental signatures to distinguish between different WCs. As an example, the collective properties at $\boldsymbol{Q} = 0$, accessible in a reflection experiment with normal incidence, are illustrated below. Fig. 3.3(a) shows $\Delta_0$ and $\Gamma_0$ for various $\nu_e$'s. In this case, the number of non-degenerate bright excitonic levels varies across the different emergent lattices. This provides the most direct fingerprints for the rectangular lattice at $\nu_e = \frac{1}{2}$ and the Kagome lattice at $\nu_e = \frac{1}{4}$, as these are the only $\nu_e$ values that exhibit two *bright* lines with equal and different $\Gamma_0$, respectively. However, distinguishing between triangular and honeycomb lattices using this bright-level counting method is rather

challenging, which motivates the utilization of the following quantitative signatures.

One quantitative optical signature for the WCs is the largest $\Gamma_0$ among all excitonic levels for a given $\nu_e$, which typically arises from the lowest level. This value generally decreases with increasing $\nu_e$ and could therefore be useful for benchmarking the appearance of corresponding WCs in experiments. Another more prominent optical fingerprint for the WCs can be obtained by observing the rate of change of $\Gamma_0$ with respect to the twisting angle $\theta$. As demonstrated in Fig. 3.3(b), $\Gamma_0/\gamma \sim N_{\nu_e}(\theta)$ for all $\theta$ and $\nu_e$, with the proportionality constant depending only on the geometry of the excitonic lattice. For example, triangular lattices at $\nu_e = 0$ and $2/3$ correspond to the same line, which differs from the lines corresponding to $\nu_e = 1/3$ and $1/4$. The observation suggests that the proportionality constant can serve as a quantitative fingerprint of the WCs.

## 3.3 Topological excitonic properties

The collective excitonic bands could also exhibit non-trivial Berry curvatures upon the introduction of an external magnetic field $B$, which adds a Zeeman splitting term $\hat{H}_B = \mu_B B \sum_{\tau,\boldsymbol{R}} \tau \hat{x}^\dagger_{\boldsymbol{R},\tau} \hat{x}_{\boldsymbol{R},\tau}$ to Eq. (3.1) and breaks time-reversal symmetry. Specifically, the right eigenvectors of the total exciton Hamiltonian, $|\boldsymbol{Q}\rangle$, are numerically evaluated to compute the Berry curvature $\Omega(\boldsymbol{Q}) = i\nabla_{\boldsymbol{Q}} \times \langle \boldsymbol{Q}|\nabla_{\boldsymbol{Q}}|\boldsymbol{Q}\rangle$. In this section, only $\Omega(\boldsymbol{Q})$ for $\boldsymbol{Q}$ within LC is considered, as these correspond to the optically accessible states.

Fig.3.4(a) shows the numerical results for a triangular lattice at $\nu_e = 0$ and a rectangular lattice at $\nu_e = 1/2$. The two excitonic bands from $\nu_e = 0$ exhibit opposite nonzero $\Omega(\boldsymbol{Q})$, both centered around $\boldsymbol{Q} = 0$. Notably, their $\Omega(\boldsymbol{Q})$ values sum (for $\boldsymbol{Q}$ within LC)

to integer values, $C_{\mathrm{LC}} = \mp 1$. This topological property arises from the phase winding of Green's tensor, Eq.(2.6), rather than being inherited from the electronic bands [71]. Specifically, this phase winding manifests in the off-diagonal terms of the following low-$\boldsymbol{Q}$ effective excitonic Hamiltonian:

$$\hat{h}(\boldsymbol{Q}) \simeq \omega_{\mathrm{ex}} + \Delta_0 - \frac{i\Gamma_0}{2} + \begin{bmatrix} \mu_B B & iJQ^2 e^{-2i\phi} \\ iJQ^2 e^{2i\phi} & -\mu_B B \end{bmatrix}, \tag{3.3}$$

where $Q$ and $\phi$ are related to the Bloch momentum as $\boldsymbol{Q} = Q(\cos\phi \boldsymbol{e}_x + \sin\phi \boldsymbol{e}_y)$, and $J$ is a complex coefficient that captures the band curvature.

On the other hand, Eq. (3.3) is not directly applicable to the rectangular lattice at $\nu = 1/2$. This is because the $C_3$ rotational symmetry is absent in this case, and therefore, nonzero off-diagonal constants emerge in addition to those in Eq. (3.3). The phase winding $Q^2 e^{-2i\phi}$ is relatively suppressed, resulting in the two bands possessing zero Berry curvature, which gives $C_{\mathrm{LC}} = 0$. Similar reasoning can be applied to other $\nu_e$'s, with the corresponding $C_{\mathrm{LC}}$ values summarized in Table 3.1.

## 3.4 Extracting band properties via optical reflectivity.

The collective spectral and topological properties of moiré excitons are proposed to be detected through far-field reflection measurements. In the following, the probing of topological features is elaborated, as the spectral properties shown in Fig. 3.3 can be directly inferred from the resonances. The setup for such measurements should be polarization-resolved and include tunability in the incident angle, which provides momentum resolution

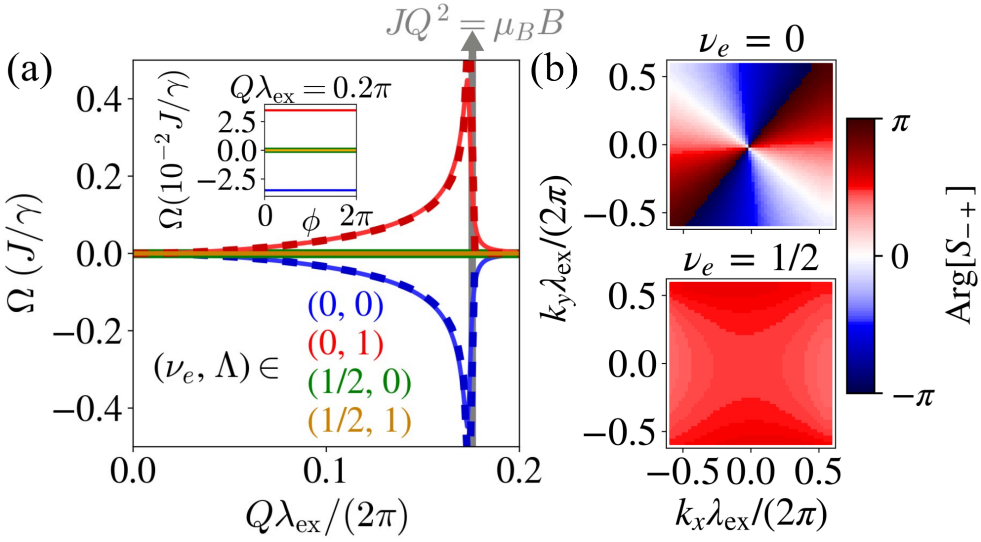


Figure 3.4: Topological and non-topological excitonic bands and their experimental signatures. (a) Dependence of Berry curvature ($\Omega$) on Bloch momentum magnitude ($Q$) for each band (labeled by $\Lambda$) at $\nu_e = 0$ and $\nu_e = \frac{1}{2}$, color-coded accordingly. Solid lines represent results from diagonalizing the full model, including Eq.(3.1)) together with a Zeeman splitting $\mu_B B = 20\gamma$, while dashed lines correspond to the low-energy model Eq.(3.3). The vertical axis is scaled by $J/\gamma$, where $J$, defined in Eq.(3.3), is obtained by fitting $\Gamma_{\boldsymbol{Q}}$ in Fig.3.2(a). The gray line indicates the momentum at which $JQ^2 = \mu_B B$. The inset shows that the dependence of $\Omega$ on the polar angle of $\boldsymbol{Q}$ is negligible. (b) Phase of the scattering matrix element $S_{-+}$ at $k = \frac{2\pi}{\lambda_{\rm ex}}$ and $\boldsymbol{k}_{||} = k_x \boldsymbol{e}_x + k_y \boldsymbol{e}_y$ for both values of $\nu_e$. Figure reproduced from Ref. [1].

(within LC). By incorporating standard homodyne techniques, both the amplitude and phase of the reflected electromagnetic field can be detected. Furthermore, by setting the incident plane-wave light to be circularly polarized and collecting the cross-polarized output fields, one can extract the corresponding scattering matrix element $S_{-+}$, which contains information about the off-diagonal term of Eq. (3.3), the source of the topological features.

To illustrate the connection between $S_{-+}$ and $\hat{h}(\boldsymbol{Q})$ with simplicity in the analysis, here the expression for this scattering matrix element for Bravais lattices (e.g., triangular

and rectangular arrays) is focused and presented below:

$$S_{-+}(\boldsymbol{k}) = \frac{3\pi c\gamma}{\omega_{\text{ex}}} \sum_{\tau} g_{-,\tau}(k, \boldsymbol{k}_{||}) D_{\tau,+}(ck, \boldsymbol{k}_{||}), \quad D_{\tau,\tau'}(\omega, \boldsymbol{Q}) = \langle \hat{x}_{\boldsymbol{Q},\tau} \left[\omega - \hat{H} - \hat{H}_B\right]^{-1} \hat{x}^{\dagger}_{\boldsymbol{Q},\tau'} \rangle. \tag{3.4}$$

Here, $\boldsymbol{k}$ denotes the momentum of the incident light, and $\boldsymbol{k}_{||}$ is its in-plane component. $g_{\tau,\tau'}(k, \boldsymbol{Q}) = -\frac{i}{2\mathcal{A}\nu_e} \frac{k^2\delta_{\tau,\tau'} - (\boldsymbol{e}^*_{\tau}\cdot\boldsymbol{Q})(\boldsymbol{e}_{\tau'}\cdot\boldsymbol{Q})}{k^2\sqrt{k^2-Q^2}}$ and $\hat{x}_{\boldsymbol{Q},\tau}$ are the momentum space representations of the Green's tensor Eq. (2.6) and $\hat{x}_{\boldsymbol{R},\tau}$, respectively. Eq. (3.4) allows for solving the exciton propagator $D_{\tau,\tau'}(\omega, \boldsymbol{Q})$, and thus the matrix elements of $\hat{H} + \hat{H}_B$, once $S_{-+}(\boldsymbol{k})$ is measured. With these Hamiltonian matrix elements, one can access the Berry curvatures, and therefore $C_{\text{LC}}$, of the excitonic bands within the LC. An important consequence of this analysis is that topological Bravais lattices possess two nodes in the phase of $S_{-+}(\boldsymbol{k})$, whereas non-topological ones have zero nodes, as illustrated in Fig. 3.4(b).

# Chapter 4: Correlations between moiré excitons: The role of nonbosonic exciton statistics

In this section, we review another theoretical framework that focuses on undoped bilayers with multipole moiré excitons, following Ref. [2]. In this analysis, the non-bosonic nature of these composite particles is incorporated into their many-body description, which is often neglected in previous studies that employ a Bose-Hubbard description [64, 72, 73]. This effect is generally non-negligible when the target exciton wavefunctions exhibit significant overlap [74, 75]. Consequently, whenever on-site repulsion between excitons arises — such as when multiple excitons occupy the same moiré unit cell — their non-bosonic nature can become significant and needs to be accounted for to obtain a correct many-body description.

## 4.1 Formulation for non-bosonic statistics of moiré excitons

The standard approach to capturing the nontrivial exciton statistics is to evaluate their commutation relations. For the lowest exciton moiré-Wannier state in Eq. (2.9), these relations take the form:

$$[\hat{x}_{\boldsymbol{R},\tau}, \hat{x}^\dagger_{\boldsymbol{R}',-\tau}] = 0; \quad (1-\delta_{\boldsymbol{R},\boldsymbol{R}'})[\hat{x}_{\boldsymbol{R},\tau}, \hat{x}^\dagger_{\boldsymbol{R}',\tau}] \simeq 0; \quad [[\hat{x}_{\boldsymbol{R},\tau}, \hat{x}^\dagger_{\boldsymbol{R},\tau}], \hat{x}^\dagger_{\boldsymbol{R},\tau}] \simeq -2\Lambda \hat{x}^\dagger_{\boldsymbol{R},\tau}. \tag{4.1}$$

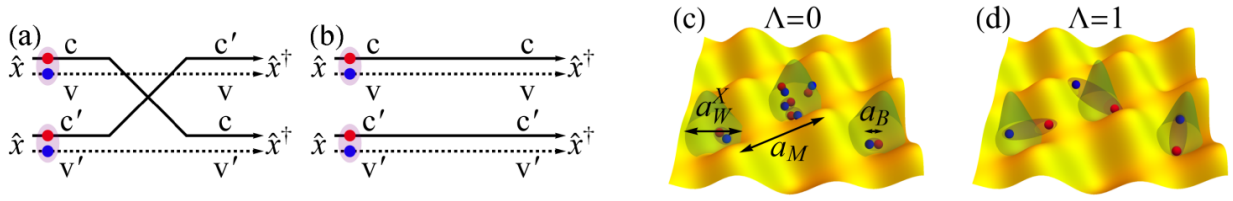


Figure 4.1: (a) Schematic of charge exchange process between two excitons ($\hat{x}$), characterized by the exchange integral $\Lambda$. In this process, two incoming excitons (purple-shaded) exchange their electrons ($c$ and $c'$, blue dots) while retaining their hole components ($v$ and $v'$, red dots). The hole-exchanged diagram is topologically equivalent. (b) Disconnected diagram representing a two-exciton process resembling free bosonic behavior. (c) Illustration of moiré excitons in a superlattice potential (yellow) when process captured in (a) is suppressed ($\Lambda = 0$), allowing unrestricted exciton occupation. This regime occurs when the exciton Wannier orbital's center-of-mass width ($a_W^x$, green peaks) is much larger than the Bohr radius ($a_B$). Here, $a_M$ denotes the superlattice constant. (d) Moiré excitons with maximal charge exchange ($\Lambda = 1$), occurring in the limit $a_W^x \ll a_B$. In this case, double occupancy per supersite and valley is prohibited. Figure reproduced from Ref. [2].

Here, the first relation follows from the fact that charges at different valleys commute by definition. The second relation arises because the overlap between exciton moiré-Wannier orbitals centered at different sites is suppressed in the regime of interest, $a_W^x, a_B \ll a_M$. In the third relation, $[\hat{x}_{\tau;\boldsymbol{R}}, \hat{x}^\dagger_{\tau;\boldsymbol{R}}]$ generally cannot be expressed compactly in terms of $\hat{x}_{\tau;\boldsymbol{R}}$ and $\hat{x}^\dagger_{\tau;\boldsymbol{R}}$, but the double commutator can be if the overlap between $w_{\boldsymbol{R}}(\boldsymbol{s}_c, \boldsymbol{s}_v)$ and higher moiré-Wannier orbitals is neglected. $\Lambda$ denotes the two-exciton exchange integral, given by:

$$\Lambda = \int d\boldsymbol{s}_c d\boldsymbol{s}_v d\boldsymbol{s}'_c d\boldsymbol{s}'_v w^*_{\boldsymbol{R}}(\boldsymbol{s}_c, \boldsymbol{s}'_v) w_{\boldsymbol{R}}(\boldsymbol{s}_c, \boldsymbol{s}_v) w_{\boldsymbol{R}}(\boldsymbol{s}'_c, \boldsymbol{s}'_v) w^*_{\boldsymbol{R}}(\boldsymbol{s}'_c, \boldsymbol{s}_v), \quad |\Lambda| \leq 1. \tag{4.2}$$

This quantity characterizes the strength of charge exchange processes between two excitons [see Fig. 4.1(a)] relative to the unexchanged channel [see Fig. 4.1(b)]. When these exchange processes are negligible, corresponding to $\Lambda \simeq 0$, the excitons recover bosonic behavior. The opposite limit, $\Lambda \simeq 1$, occurs when $w_{\boldsymbol{R}}(\boldsymbol{s}_c, \boldsymbol{s}_v)$ is nearly a product state of a CMB electron

and a VMB hole, leading to $(\hat{x}^\dagger_{\boldsymbol{R},\tau}) \simeq (\hat{c}^\dagger_{\boldsymbol{R},\tau}\hat{v}^\dagger_{\boldsymbol{R},\tau})^2 = 0$. These considerations indicate that $\Lambda$ also characterizes the extent to which moiré excitons inherit Pauli exclusion from their charge constituents.

The last commutator in Eq. (4.1) also suggests a connection between $\hat{x}_{\boldsymbol{R},\tau}$ and angular momentum operators satisfying $[\hat{\mathcal{S}}^+_{\boldsymbol{R},\tau}, \hat{\mathcal{S}}^-_{\boldsymbol{R},\tau}] = 2\hat{\mathcal{S}}^z_{\boldsymbol{R},\tau}$ and $[\hat{\mathcal{S}}^z_{\boldsymbol{R},\tau}, \hat{\mathcal{S}}^-_{\boldsymbol{R},\tau}] = -\hat{\mathcal{S}}^-_{\boldsymbol{R},\tau}$. Specifically, the above algebra is satisfied if one replaces:

$$\frac{\hat{x}^\dagger_{\boldsymbol{R},\tau}}{\sqrt{\Lambda}} = \hat{\mathcal{S}}^-_{\boldsymbol{R},\tau}, \ \frac{\hat{x}_{\boldsymbol{R},\tau}}{\sqrt{\Lambda}} = \hat{\mathcal{S}}^+_{\boldsymbol{R},\tau}, \ \frac{[\hat{x}_{\boldsymbol{R},\tau}, \hat{x}^\dagger_{\boldsymbol{R},\tau}]}{2\Lambda} = \hat{\mathcal{S}}^z_{\boldsymbol{R},\tau}. \tag{4.3}$$

Notably, the eigenvalues of $\hat{\mathcal{S}}^z_{\boldsymbol{R},\tau}$ do not have to be integers or half-integers, as this set of emergent angular momentum operators does not correspond to the generators of rotations. The state with the largest $\hat{\mathcal{S}}^z_{\boldsymbol{R},\tau}$ eigenvalue, $(2\Lambda)^{-1}$, corresponds to the vacuum state of the exciton. Eq. (4.3) also implies that $\hat{x}_{\boldsymbol{R},\tau}$ can be mapped onto an emergent bosonic degree of freedom $\hat{a}_{\boldsymbol{R},\tau}$ via a Holstein-Primakoff transformation [76]:

$$\hat{x}_{\boldsymbol{R},\tau} \simeq \theta(1 - \Lambda\hat{a}^\dagger_{\boldsymbol{R},\tau}\hat{a}_{\boldsymbol{R},\tau}) \sqrt{1 - \Lambda\hat{a}^\dagger_{\boldsymbol{R},\tau}\hat{a}_{\boldsymbol{R},\tau}} \, \hat{a}_{\boldsymbol{R},\tau}, \tag{4.4}$$

where the Heaviside step function $\theta(x)$ is included to ensure that the argument inside the square root remains non-negative.

The representation in Eq. (4.4) suggests that exciton occupancy at each $(\boldsymbol{R}, \tau)$ is bounded below:

$$\nu_{\max} = \mathrm{ceil}(\Lambda^{-1}), \quad (\hat{x}_{\tau;\boldsymbol{R}})^{\nu_{\max}+1} = 0, \tag{4.5}$$

where $\mathrm{ceil}(x)$ denotes the ceiling function, which returns the smallest integer greater than

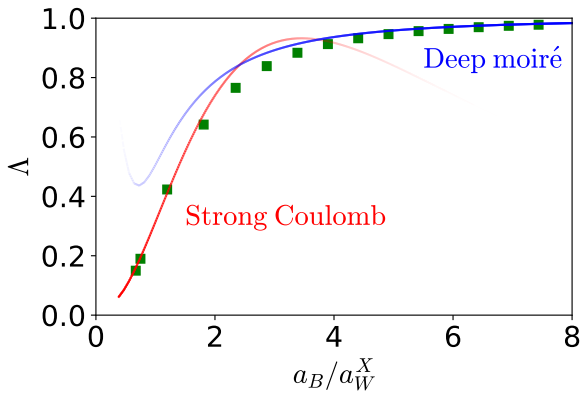


Figure 4.2: Exchange integral $\Lambda$ as a function of $a_B/a_W^x$ for intralayer excitons. Green points represent numerical results from Eq. (2.8). The red and blue curves correspond to results from perturbative wavefunctions in the strong Coulomb and deep moiré regimes, respectively. The opacity indicates their respective regions of validity. Figure reproduced from Ref. [2], and is generated using parameters from untwisted $WSe_2/WS_2$.

or equal to $x$. This saturation effect, known as *phase space filling* (PSF), is present for all non-bosonic excitons. Eq. (4.5) can be interpreted as follows: While $\nu_{\max}$ is largely unrestricted at small $\Lambda$ [see Fig. 4.1(c)], it decreases with $\Lambda$ and reaches the most restrictive case, $\nu_{\max} = 1$, when $\Lambda = 1$ [see Fig. 4.1(d)]. Notably, as $\Lambda$ also characterizes the extent to which an exciton inherits the Pauli exclusion from its constituent charges, this fermionic effect can be interpreted as the underlying mechanism of PSF.

The strength of this blockade effect generally depends on the ratio $a_B/a_W^x$. Fig. 4.2 shows that $\Lambda$ increases with this ratio for intralayer excitons within an R-stacked bilayer, where wavefunctions are obtained from the numerical solution of Eq. (2.8) under the assumption $\Delta_c(\boldsymbol{s}) = \Delta_v(\boldsymbol{s})$. This result can be understood by considering the behaviors in the strong Coulomb and deep moiré regimes. As the system approaches the strong Coulomb regime ($a_W^x \gg a_B$), charge exchange between two excitons needs to overcome the strong binding energy and is therefore suppressed. Accordingly, $\Lambda \to 0$ as $a_B/a_W^x \to 0$, resulting in nearly bosonic excitons with an unrestricted occupation number [see Fig. 4.1(c)]. In

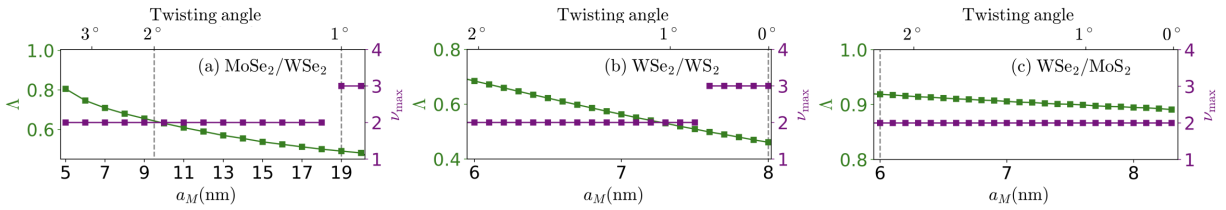


Figure 4.3: Exchange integral $\Lambda$ and occupancy upper bound $\nu_{\max}$ for interlayer excitons in R-stacked TMD bilayers at various twisting angles. Dashed vertical lines indicate twisting angles reported in the literature [57, 53, 77]. Figure reproduced from Ref. [2].

contrast, in the deep moiré limit ($a_W^x \ll a_B$), the weak electron-hole binding allows the charge exchange process to become comparable to the unscattered process [see Fig. 4.1(b)], leading to a larger $\Lambda$ that saturates at 1. These interpretations of the numerical results are consistent with the analytical solutions in these regimes.

Physically, the ratio $a_B/a_W^x$ is determined by the moiré period $a_M$ along with other material parameters. Fig. 4.3 presents $\Lambda$ and $\nu_{\max}$ for interlayer excitons in different R-stacked bilayers at various superlattice spacings. These materials and twisting angles generally yield $1/3 < \Lambda < 1$, corresponding to $3 \geq \nu_{\max} \geq 2$. This result suggests that PSF is non-negligible for moiré excitons and demonstrates that their statistics typically lies in an intermediate regime between the bosonic and Pauli limits. Another important feature is that larger $\Lambda$ and smaller $\nu_{\max}$ can be achieved by accessing a smaller $a_M$, or equivalently, a larger twisting angle. Since a smaller $a_M$ typically leads to a smaller $a_W^x$ while $a_B$ remains unchanged, the above results are consistent with the previous discussion on $a_B/a_W^x$.

## 4.2 Effective model: multiple interacting excitons without doped charges

An interacting exciton model incorporating nonbosonicity can be derived from the electron-photon parent Hamiltonian $\hat{\mathcal{H}}$. Several assumptions are made in this derivation. First,

higher excitonic orbitals are neglected, which is strictly valid only if their energies are greater than $E_0 + U_{\mathrm{ex}}$, where $E_0$ denotes the single-exciton occupation energy and $U_{\mathrm{ex}}$ represents the on-site two-body repulsion. In addition, only the nearest-neighbor exciton tunneling arising from intrinsic charge motion, denoted as $t_{\mathrm{ex}}$, is retained for simplicity ($\hat{\mathcal{V}}_d$ is suppressed at this point, and its role will be discussed later). Finally, the condition $|t_{\mathrm{ex}}| \ll U_{\mathrm{ex}}$ is assumed to be consistent with the approximation of neglecting off-site exciton commutators in Eq. (4.1). With these considerations, the effective excitonic Hamiltonian takes the following form in the emergent-boson representation:

$$\begin{aligned}\hat{\mathcal{H}}_{\mathrm{eff}} = & E_0 \sum_{\boldsymbol{R},\tau} \hat{a}^\dagger_{\tau;\boldsymbol{R}} \hat{a}_{\tau;\boldsymbol{R}} - t_{\mathrm{ex}} \sum_{\langle \boldsymbol{R}',\boldsymbol{R}\rangle} (\hat{a}^\dagger_{\tau;\boldsymbol{R}'} \hat{a}_{\tau;\boldsymbol{R}} + \mathrm{H.c.}) \\ & + \frac{U_{\mathrm{ex}}}{2} \sum_{\boldsymbol{R},\tau,\tau'} \hat{a}^\dagger_{\tau;\boldsymbol{R}} \hat{a}^\dagger_{\tau';\boldsymbol{R}} \hat{a}_{\tau';\boldsymbol{R}} \hat{a}_{\tau;\boldsymbol{R}} + \lim_{\tilde{U}_{\mathrm{ex}}\to\infty} \tilde{U}_{\mathrm{ex}} \sum_{\boldsymbol{R},\tau} (\hat{a}^\dagger_{\tau;\boldsymbol{R}})^{\nu_{\max}+1} (\hat{a}_{\tau;\boldsymbol{R}})^{\nu_{\max}+1}.\end{aligned} \tag{4.6}$$

Note the presence of an infinite $(\nu_{\max}+1)$-body interaction $\tilde{U}_{\mathrm{ex}}$ that originates from PSF. This additional term introduces a qualitative change in the excitonic phase diagram compared to the standard Bose-Hubbard model. In particular, when the exciton occupation exceeds $\nu_{\max}$, the many-body state becomes incompressible regardless of $t_{\mathrm{ex}}$.

In addition, PSF renormalizes the optical matrix elements of moiré excitons, thereby modifying the light-matter interaction $\hat{\mathcal{H}}_T$. Following Eq. (2.4), electromagnetic fields couple linearly to $\hat{x}_{\boldsymbol{R},\tau}$ and, consequently, nonlinearly to $\hat{a}_{\boldsymbol{R},\tau}$. This nonlinearity manifests as a suppression factor in the following transition matrix element:

$$\langle \nu+1|\hat{x}^\dagger_{\boldsymbol{R},\tau}|\nu\rangle = \theta(\nu_{\max}-\nu)\sqrt{(\nu+1)(1-\Lambda\nu)}, \quad |\nu\rangle = \frac{1}{\sqrt{\nu!}}(\hat{a}^\dagger_{\boldsymbol{R},\tau})^\nu|\mathrm{vac}\rangle, \tag{4.7}$$

which is generally weaker than that for bosonic excitations, $\sqrt{\nu+1}$. In other words, optically driving moiré excitons with greater nonbosonicity is generally more challenging.

## 4.3 Experimental signatures of non-bosonicity

The validity of the interacting high-order hardcore boson model, Eq. (4.6), can be tested by examining photoluminescence at high pump power [53]. Since the energy of a $\nu$-exciton state is given by $\nu E_0 + \frac{\nu(\nu-1)}{2} U_{\text{ex}}$, emission at frequencies $E_0$, $E_0 + U_{\text{ex}}$, $E_0 + 2U_{\text{ex}}$, ... would sequentially appear as the pump power increases, up to $E_0 + (\nu_{\max} - 1)U_{\text{ex}}$, which is a manifestation of PSF. Beyond this critical power, higher moiré-Wannier excitonic states are accessed, and the splitting between emission peaks is generally no longer $U_{\text{ex}}$. These predictions serve as a signature of excitonic nonbosonicity and are consistent with measurements for $WSe_2/WS_2$ [53].

# Chapter 5: Moiré excitons coexisting with spin-ordered states of doped electrons

Finally, we review how a single moiré exciton can interplay with the spin degrees of freedom of doped charges, following Ref. [3]. The system considered here consists of an initially half-filled VMB (one hole per moiré unit cell) in an R-stacked heterobilayer, forming a Mott insulator described by the Fermi-Hubbard model. At zero temperature, theoretical predictions suggest that this system hosts a frustrated antiferromagnetic order [26, 78, 79]. On top of this configuration, a VMB electron is transferred to the CMB, leaving behind a vacant site (referred to as a "holon") in the VMB. The motion of the holon disturbs the background, generating spin fluctuations that, in turn, dress its dynamics into a magnetic polaron state [80, 81, 82, 4]. This quasiparticle can then bind to the CMB electron via electrostatic attraction, forming the target excitonic state of this section, as illustrated in Fig. 5.1.

## 5.1 Effective model: single-exciton on top of half-filled doped holes

The effective Hamiltonian describing one CMB electron and multiple VMB holes can be derived from the parent Hamiltonian $\hat{\mathcal{H}}$, following similar steps as in Section 2.2.1. Additionally, for simplicity, the excitonic tunneling induced by light-matter coupling $\hat{\mathcal{V}}_d$ is

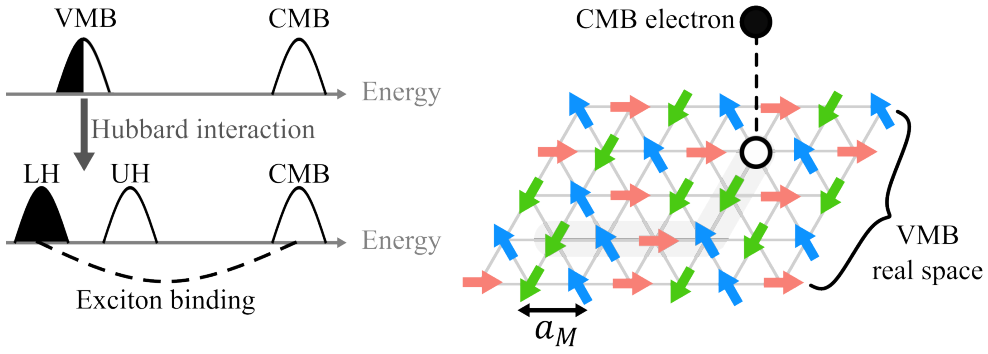


Figure 5.1: Left: Illustration of density of states at the conduction and valence moiré bands (CMB and VMB). The vertical axis represents energy, with the shaded region indicating the filled Fermi sea. Strong Hubbard interaction within VMB splits it into upper and lower Hubbard bands (UH and LH). Black wavy lines illustrate interactions that give rise to the target exciton. Right: Schematic of an exciton coexisting with a magnetic order in VMB. Black and white dots represent CMB electron and VMB hole, respectively. Red, green, and blue arrows depict the 120° spin-ordered state on the triangular moiré superlattice in VMB. The trajectory of the hole (gray shading) perturbs the spin order as it moves. Figure reproduced from Ref. [3].

suppressed. This suppression can be achieved by reducing the transition dipole of the target electron-hole pair, which may result from the application of an out-of-plane electric field if the CMB electrons and VMB holes reside in different layers. With these considerations, and retaining only nearest-neighbor terms in charge hopping and the on-site contribution of the Hubbard repulsion for simplicity, the effective Hamiltonian takes the following form:

$$\begin{aligned} \hat{H} &= \hat{H}^v_{\text{Hub}} - t\sum_{\tau}\sum_{\langle \boldsymbol{R},\boldsymbol{R}'\rangle} \hat{c}^\dagger_{\boldsymbol{R},\tau}\hat{c}_{\boldsymbol{R}',\tau} - \sum_{\tau,\tau'}\sum_{\boldsymbol{R},\boldsymbol{R}'} V_{|\boldsymbol{R}-\boldsymbol{R}'|}\hat{c}^\dagger_{\boldsymbol{R},\tau}\hat{v}^\dagger_{\boldsymbol{R}',\tau'}\hat{v}_{\boldsymbol{R}',\tau'}\hat{c}_{\boldsymbol{R},\tau} \\ \hat{H}^v_{\text{Hub}} &= -t\sum_{\tau}\sum_{\langle \boldsymbol{R},\boldsymbol{R}'\rangle} \hat{v}^\dagger_{\boldsymbol{R},\tau}\hat{v}_{\boldsymbol{R}',\tau} + U_v\sum_{\boldsymbol{R}} \hat{v}^\dagger_{\boldsymbol{R},+}\hat{v}^\dagger_{\boldsymbol{R},-}\hat{v}_{\boldsymbol{R},-}\hat{v}_{\boldsymbol{R},+}, \end{aligned} \tag{5.1}$$

where $\langle \boldsymbol{R}, \boldsymbol{R}'\rangle$ denotes nearest-neighbor sites on a triangular superlattice, and recall that $\hat{c}_{\boldsymbol{R},\tau}$ and $\hat{v}_{\boldsymbol{R},\tau}$ represent the annihilation operators of the CMB electron and VMB hole, respectively. Here, the tunneling of these two charges is assumed to be identical, denoted

by $t$, for simplicity. $U_v$ and $V_{|\boldsymbol{R}-\boldsymbol{R}'|}$ represent the on-site repulsion between VMB charges and the off-site attraction between CMB electrons and VMB holes, respectively.

Near half-filling of the VMB, along with the dilute CMB electron condition and considering the typical regime for moiré TMDs where $|t| \ll U_v$, the sector $\hat{H}^v_{\text{Hub}}$ becomes the following effective t-J model after applying a standard perturbation method [76]:

$$\hat{H}_{\text{tJ}} = -t\sum_{\tau}\sum_{\langle \boldsymbol{R},\boldsymbol{R}'\rangle} \hat{\mathcal{P}}\hat{h}^{\dagger}_{\boldsymbol{R},\tau}\hat{h}_{\boldsymbol{R}',\tau}\hat{\mathcal{P}} + \hat{H}_J, \quad \hat{H}_J = J\sum_{\langle \boldsymbol{R},\boldsymbol{R}'\rangle} \hat{\boldsymbol{S}}_{\boldsymbol{R}}\cdot\hat{\boldsymbol{S}}_{\boldsymbol{R}'}, \quad \hat{\boldsymbol{S}}_{\boldsymbol{R}} \equiv \sum_{\tau\tau'}\hat{h}_{\boldsymbol{R},\tau}\frac{\boldsymbol{\sigma}_{\tau,\tau'}}{2}\hat{h}^{\dagger}_{\boldsymbol{R},\tau'}, \tag{5.2}$$

where $J = \frac{4t^2}{U_v}$ is the superexchange energy scale. The projection operator $\hat{\mathcal{P}}$ excludes states with double occupancies of VMB electrons at any moiré site. $\boldsymbol{\sigma}_{\tau,\tau'}$ is the three-component vector representing the matrix elements of the Pauli operators. For triangular lattices, $\hat{H}_J$ favors a 120° coplanar spin order, as illustrated in Fig. 5.1. The magnetic excitations from this order are characterized by $J$, which is significantly slower than the bare charge dynamics $\sim t$. Since these fluctuations couple to the VMB holon via Eq. (5.2), the propagation rate of their composite object, referred to as "magnetic polarons" or "spin polarons" [80, 81, 82], is reduced to $J$.

Several analytical approaches are employed to describe the behavior of charge and spin in the VMB, as discussed in the following.

### 5.1.1 Slave-fermion representation of the t-J model

First, the slave-fermion representation for the VMB hole is utilized, as it conveniently separates the charge and spin degrees of freedom. Specifically, as pictorially illustrated in Fig. 5.2(a), in the zero-double-occupancy subspace, $\hat{h}_{\boldsymbol{R},\tau}$ can be replaced by the product of a

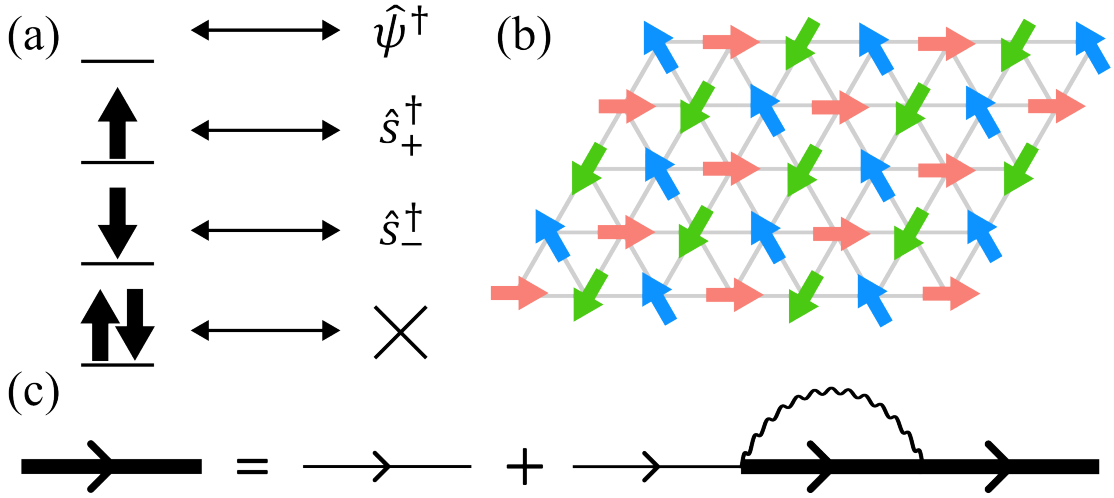


Figure 5.2: Illustration of the analytical treatments. (a) Schematic representation of the slave-particle formalism. Up- and down-arrows denote states occupied by a single $\tau = +$ or $\tau = -$ VMB electron, respectively, which are mapped to corresponding bosonic spinons ($\hat{s}$). States with zero and two electrons are mapped to fermionic slave particles: holons ($\hat{\psi}$) and doublons. Doublons are not shown, as indicated by the cross, since they are energetically unfavorable. (b) Classical mean-field ground state from the triangular lattice antiferromagnetic Heisenberg model exhibits a 120° coplanar magnetic order. Colors indicate the directions of spin vectors and their corresponding sublattices. (c) Diagrammatic equation for the self-consistent Born approximation (SCBA) applied to the holon propagator. Thin solid single lines represent the bare holon propagator, while bold solid lines denote the dressed holon propagator. The wiggly curve corresponds to the propagator of a spin excitation.

creation operator for a bosonic "spinon" $\hat{s}^\dagger_{\boldsymbol{R},\tau}$ and an annihilation operator for a fermionic "holon" $\hat{\psi}_{\boldsymbol{R}}$ [83, 84, 85]. This substitution is accompanied by the constraint $\hat{\psi}^\dagger_{\boldsymbol{R}}\hat{\psi}_{\boldsymbol{R}} + \sum_\tau \hat{s}^\dagger_{\boldsymbol{R},\tau}\hat{s}_{\boldsymbol{R},\tau} = 1$, which is essential for preserving the Hilbert space size under the slave-particle transformation. This approach yields the following representation of the t-J model:

$$\hat{H}_{\mathrm{tJ}} = -t\sum_\tau \sum_{\langle \boldsymbol{R},\boldsymbol{R}'\rangle} \left(\hat{\psi}^\dagger_{\boldsymbol{R}}\hat{\psi}_{\boldsymbol{R}'}\hat{s}^\dagger_{\boldsymbol{R}',\tau}\hat{s}_{\boldsymbol{R},\tau} + h.c.\right) + J\sum_{\langle \boldsymbol{R},\boldsymbol{R}'\rangle} \hat{\boldsymbol{S}}_{\boldsymbol{R}}\cdot\hat{\boldsymbol{S}}_{\boldsymbol{R}'},\ \ \hat{\boldsymbol{S}}_{\boldsymbol{R}} = \sum_{\tau\tau'} \hat{s}^\dagger_{\boldsymbol{R},\tau}\frac{\hat{\boldsymbol{\sigma}}_{\tau,\tau'}}{2}\hat{s}_{\boldsymbol{R},\tau'}. \tag{5.3}$$

Note that the $J$ term is constructed solely from spinon operators in this representation.

### 5.1.2 Mean field description for magnetic order

To proceed, it is assumed that the magnetic ground state is primarily determined by the $J$ term in Eq. (5.3). Using a classical mean-field treatment, the lowest-energy state yields:

$$\langle \hat{\boldsymbol{\mathcal{S}}}_{\boldsymbol{R}} \rangle = \frac{\hat{\boldsymbol{n}}_{\boldsymbol{R}}}{2}, \quad \hat{\boldsymbol{n}}_{\boldsymbol{R}} = \begin{cases} \boldsymbol{e}_x, & \boldsymbol{R} \in A \\ -\frac{\boldsymbol{e}_x}{2} - \frac{\sqrt{3}\boldsymbol{e}_y}{2}, & \boldsymbol{R} \in B \\ -\frac{\boldsymbol{e}_x}{2} + \frac{\sqrt{3}\boldsymbol{e}_y}{2}, & \boldsymbol{R} \in C \end{cases}, \tag{5.4}$$

where $A$, $B$, and $C$ indicate the three sublattices illustrated in Fig. 5.2(b). Fluctuations on top of this ordered state are incorporated using the following rotated Holstein-Primakoff representation of spinons [76]:

$$\begin{bmatrix} \hat{s}_{\boldsymbol{R}\uparrow} \\ \hat{s}_{\boldsymbol{R}\downarrow} \end{bmatrix} = \hat{U}_{\boldsymbol{R}} \begin{bmatrix} \sqrt{1 - \hat{b}^\dagger_{\boldsymbol{R}} \hat{b}_{\boldsymbol{R}}} \\ \hat{b}_{\boldsymbol{R}} \end{bmatrix}, \tag{5.5}$$

where $\hat{U}_{\boldsymbol{R}}$ is the spin rotation matrix that rotates $\hat{\boldsymbol{n}}_{\boldsymbol{R}}$ to $\boldsymbol{e}_z$. $\hat{b}_{\boldsymbol{R}}$ denotes the annihilation operator of the Holstein-Primakoff bosons. Note that the transformation in Eq. (5.5) is exact, and the classical mean-field theory corresponds to the limit $\hat{b}_{\boldsymbol{R}} \to 0$. This treatment can be improved by replacing $\sqrt{1 - \hat{b}^\dagger_{\boldsymbol{R}} \hat{b}_{\boldsymbol{R}}}$ in the above expression with $\xi \equiv \sqrt{1 - \frac{1}{N} \sum_{\boldsymbol{R}} \langle \hat{b}^\dagger_{\boldsymbol{R}} \hat{b}_{\boldsymbol{R}} \rangle}$, where $\langle \hat{b}^\dagger_{\boldsymbol{R}} \hat{b}_{\boldsymbol{R}} \rangle$ is the ground-state expectation value, to be determined self-consistently later. Under these steps, $\hat{H}_J$ becomes a quadratic Hamiltonian, and takes the following form after

a Fourier transform to momentum space followed by a Bogoliubov rotation:

$$\hat{H}_J = \frac{3J\xi^2}{2}\sum_{\boldsymbol{q}} \Omega_{\boldsymbol{q}} \hat{\beta}^\dagger_{\boldsymbol{q}} \hat{\beta}_{\boldsymbol{q}}, \quad \hat{\beta}_{\boldsymbol{q}} \equiv u_{\boldsymbol{q}} \hat{b}_{\boldsymbol{q}} - v_{\boldsymbol{q}} \hat{b}^\dagger_{-\boldsymbol{q}}, \quad \Omega_{\boldsymbol{q}} = \sqrt{\left(1+\frac{\gamma_{\boldsymbol{q}}}{6}\right)^2 - \frac{\gamma^2_{\boldsymbol{q}}}{4}}, \tag{5.6}$$

where $\hat{b}_{\boldsymbol{q}}$ is the momentum-space ($\boldsymbol{q}$) representation of $\hat{b}_{\boldsymbol{R}}$, and:

$$\gamma_{\boldsymbol{q}} = \sum_{i=1}^{3} \cos(a_M \boldsymbol{q}\cdot\boldsymbol{e}_i), \quad u_{\boldsymbol{q}} = \sqrt{\frac{1}{2\Omega_{\boldsymbol{q}}}\left(1+\frac{\gamma_{\boldsymbol{q}}}{6}+\Omega_{\boldsymbol{q}}\right)}, \quad v_{\boldsymbol{q}} = \mathrm{sgn}[\gamma_{\boldsymbol{q}}]\sqrt{\frac{1}{2\Omega_{\boldsymbol{q}}}\left(1+\frac{\gamma_{\boldsymbol{q}}}{6}-\Omega_{\boldsymbol{q}}\right)}, \tag{5.7}$$

with $\boldsymbol{e}_1 = \boldsymbol{e}_x$ and $\boldsymbol{e}_{2,3} = -\boldsymbol{e}_x/2 \pm \sqrt{3}\boldsymbol{e}_y/2$. The ground state of Eq. (5.6) yields the self-consistent solution $\xi \simeq 0.86$, or equivalently, the normalized sublattice magnetization $m \equiv 1 - \frac{1}{N}\sum_{\boldsymbol{R}} \langle \hat{b}^\dagger_{\boldsymbol{R}} \hat{b}_{\boldsymbol{R}} \rangle \simeq 0.48$ (recall $N = \sum_{\boldsymbol{R}} 1$). Notably, this order parameter is independent of $t$ and $U$.

Applying a similar treatment to the hopping term in Eq. (5.3) yields:

$$\hat{H}_{\mathrm{tJ}} = t\xi^2 \sum_{\boldsymbol{k}} \gamma_{\boldsymbol{k}} \hat{\psi}^\dagger_{\boldsymbol{k}} \hat{\psi}_{\boldsymbol{k}} + \frac{\sqrt{3}t\xi}{\sqrt{N}} \sum_{\boldsymbol{k},\boldsymbol{q}} \left[ i M_{\boldsymbol{k},\boldsymbol{q}} \hat{\psi}^\dagger_{\boldsymbol{k}+\boldsymbol{q}} \hat{\psi}_{\boldsymbol{k}} \hat{\beta}^\dagger_{-\boldsymbol{q}} + h.c. \right] + \frac{3J\xi^2}{2} \sum_{\boldsymbol{q}} \Omega_{\boldsymbol{q}} \hat{\beta}^\dagger_{\boldsymbol{q}} \hat{\beta}_{\boldsymbol{q}}, \tag{5.8}$$

$$M_{\boldsymbol{k},\boldsymbol{q}} = h_{\boldsymbol{k}} v_{\boldsymbol{q}} - h_{\boldsymbol{k}+\boldsymbol{q}} u_{\boldsymbol{q}}, \quad h_{\boldsymbol{k}} \equiv \sum_{i=1}^{3} \sin(a_M \boldsymbol{k}\cdot\boldsymbol{e}_i). \tag{5.9}$$

### 5.1.3 Diagrammatic calculation for magnetic polaron

To compute the dressed holon propagator from Eq. (5.8), a diagrammatic approach is employed together with the standard self-consistent Born approximation (SCBA) [80, 78, 86, 79], as illustrated in Fig. 5.2(c). This approximation neglects diagrams that violate the slave-particle constraint or describe processes in which the holon circulates around moiré

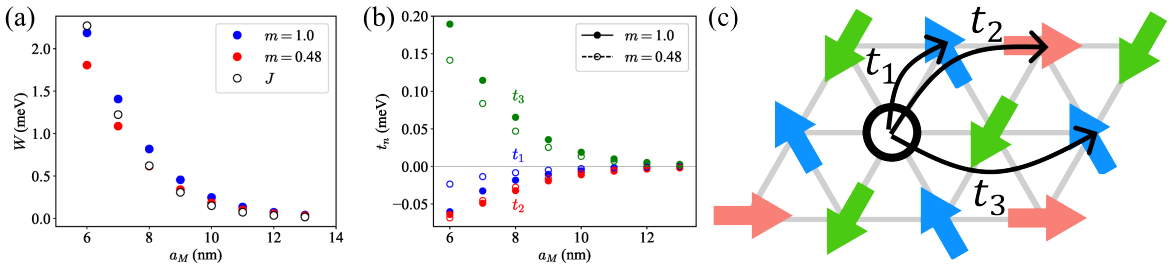


Figure 5.3: Properties from the dressed holon dispersion. (a) Holon bandwidth $W$ computed via SCBA as a function of the moiré period $a_M$. For comparison, the exchange coupling $J$ (empty circles) is also shown as a function of $a_M$, using parameters for $WSe_2/MoSe_2$ from Ref.[26]. (b) Fitted hopping parameters $t_1$, $t_2$, and $t_3$ from the dressed holon dispersion in Eq.(5.11), plotted as functions of $a_M$. Data for two sublattice magnetizations, $m = 1$ and $m = 0.48$, are shown. The system size used is $3 \times 24^2$ sites. (c) Schematic illustration of effective holon hopping (white dot) within the 120° spin-ordered background. Panels (a) and (b) reproduced from Ref. [3].

unit cells [80]. Mathematically, it leads to the following self-consistent equation for the holon self-energy $\Sigma_{\boldsymbol{k}}(\epsilon)$:

$$\Sigma_{\boldsymbol{k}}(\epsilon) = \frac{3t^2\xi^2}{N} \sum_{\boldsymbol{q}} \frac{M^2_{\boldsymbol{k},\boldsymbol{q}}}{\epsilon - \omega_{\boldsymbol{q}} - t\xi^2\gamma_{\boldsymbol{k}+\boldsymbol{q}} - \Sigma_{\boldsymbol{k}+\boldsymbol{q}}(\epsilon - \omega_{\boldsymbol{q}})}, \tag{5.10}$$

where $\epsilon$ is the frequency argument of the self-energy. The dressed holon dispersion can be obtained by numerically solving $\Sigma_{\boldsymbol{k}}(\epsilon_{\boldsymbol{k}}) + t\xi^2\gamma_{\boldsymbol{k}} = \epsilon_{\boldsymbol{k}}$. The solution can be well approximated by the following expression:

$$\epsilon_{\boldsymbol{k}} = -2\sum_{i=1}^{3} \left[ t_1 \cos(a_M \boldsymbol{k}\cdot\boldsymbol{e}_i) + t_2 \cos(a_M \boldsymbol{k}\cdot\boldsymbol{e}'_i) + t_3 \cos(2a_M \boldsymbol{k}\cdot\boldsymbol{e}_i) \right], \tag{5.11}$$

where $\boldsymbol{e}'_1 = \sqrt{3}\boldsymbol{e}_y$ and $\boldsymbol{e}'_{2,3} = \pm\frac{3}{2}\boldsymbol{e}_x - \frac{\sqrt{3}}{2}\boldsymbol{e}_y$, and recall that $\boldsymbol{e}_1 = \boldsymbol{e}_x$ and $\boldsymbol{e}_{2,3} = -\boldsymbol{e}_x/2 \pm \sqrt{3}\boldsymbol{e}_y/2$. The hopping integrals $t_1$, $t_2$, and $t_3$ can be interpreted as the nearest-neighbor, next-nearest-neighbor, and third-nearest-neighbor holon tunnelings, respectively, as illustrated in Fig. 5.3(c).

Fig. 5.3 presents the numerical results from Eq. (5.10). First, the dressed holon bandwidth scales with $J$, consistent with the magnetic polaron picture [82]. Accordingly, the effective hopping parameters satisfy $|t_1|, |t_2|, |t_3| \ll |t|$. All of these energy scales decrease with increasing $a_M$, which originates from the more reduced overlap between electronic moiré-Wannier orbitals at nearest-neighbor sites [26]. Note that both the self-consistent sublattice magnetization $m \simeq 0.48$ and the classical value $m = 1$ are shown as a comparison, which indicates that changes in the magnetic order lead only to quantitative differences.

### 5.1.4 Two-body bound state between a magnetic polaron and a free electron

The dressed holon dispersion $\epsilon_{\boldsymbol{k}}$, the CMB electron kinetic energy $-2t\gamma_{\boldsymbol{k}}\hat{c}^{\dagger}_{\boldsymbol{k},\tau}\hat{c}_{\boldsymbol{k},\tau}$, and the electron-hole electrostatic attraction together constitute the following two-body Schrödinger equation:

$$\left(\epsilon_{\frac{\boldsymbol{Q}}{2}-\boldsymbol{p}} - 2t\gamma_{\frac{\boldsymbol{Q}}{2}+\boldsymbol{p}}\right)\Phi_{\boldsymbol{Q}}(\boldsymbol{p}) - \frac{2\pi e^2}{N\epsilon_r \mathcal{A}}\sum_{\boldsymbol{q}}\frac{\tanh(qz_s)}{q}\Phi_{\boldsymbol{Q}}(\boldsymbol{p}-\boldsymbol{q}) = \mathcal{E}_{\boldsymbol{Q}}\Phi_{\boldsymbol{Q}}(\boldsymbol{p}). \tag{5.12}$$

Here, $\frac{\tanh(qz_s)}{q}$ characterizes the momentum-space representation of the dual-gate screened electron-hole attraction, which can be achieved by incorporating metallic gates at a vertical distance $z_s$ from the bilayer [87, 88]. Note that the results are largely insensitive to $z_s$ in the regime $z_s \gg a_M$. $\epsilon_r$ denotes the dielectric constant arising from static screening, and recall that $N$ and $\mathcal{A}$ are the number of supersites and the moiré unit cell area, respectively. The solution to the above equation yields the exciton energies $\mathcal{E}_{\boldsymbol{Q}}$ and wavefunctions $\Phi_{\boldsymbol{Q}}(\boldsymbol{p})$,

expressed in terms of center-of-mass and relative momenta, denoted $\boldsymbol{Q}$ and $\boldsymbol{p}$, respectively. Note that internal-state and CMB-valley labels are suppressed for simplicity.

Eq. (5.12) can be solved perturbatively by considering the typical regime in which the binding interaction is much stronger than the charge tunnelings. Specifically, denoting the electrostatic attraction energies between on-site and nearest-neighbor electron-hole pairs as $V_0$ and $V_1$, respectively (with $V_0 \gg V_1$ typically), second-order perturbation theory gives $\mathcal{E}_{\boldsymbol{Q}} \simeq [-V_0 + \mathcal{O}(J)] - \frac{4tt_1}{V_0 - V_1}\gamma_{\boldsymbol{Q}}$. The corresponding bandwidth for a Mott exciton embedded in the magnetic order described by Eq. (5.4) is therefore $W_X^{MO} \simeq \frac{18|tt_1|}{V_0 - V_1}$. A similar analysis for an exciton in a paramagnetic state, where $\epsilon_{\frac{\boldsymbol{Q}}{2}-\boldsymbol{p}}$ in Eq. (5.12) is replaced by $-2t\gamma_{\frac{\boldsymbol{Q}}{2}-\boldsymbol{p}}$, yields a bandwidth of $W_X^{PM} \simeq \frac{18t^2}{V_0 - V_1}$.

## 5.2 Experimental signatures for magnetically dressed moiré exciton

The analysis in the previous section demonstrates that the magnetic polaron effect suppresses the excitonic bandwidth by a factor of $\frac{W_X^{MO}}{W_X^{PM}} \simeq |\frac{t_1}{t}|$, which qualitatively originates from a similar suppression in the holon bandwidth. This perturbative result is consistent with numerical calculations of the lowest excitonic state obtained by diagonalizing Eq. (5.12), as illustrated in Fig. 5.4. By substituting parameters for a realistic bilayer system (here, $MoSe_2/WSe_2$), it is found that the excitonic bandwidth reduction is orders of magnitude and persists across a range of experimentally relevant moiré periods. This provides a robust qualitative signature to distinguish excitonic species arising from magnetic order versus those from a paramagnetic background.

Such a signature could potentially be extracted from excitonic diffusion measure-

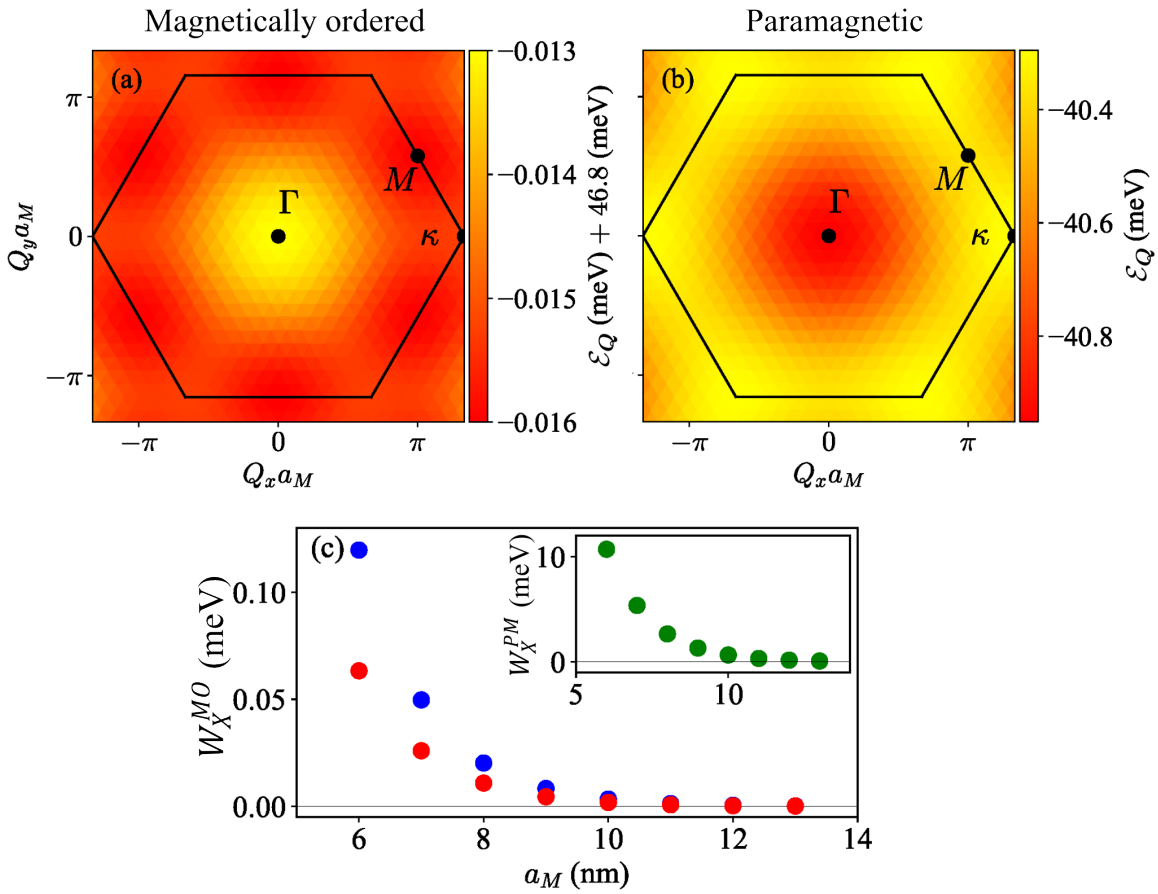


Figure 5.4: Dispersion of the lowest excitonic state in (a) a magnetically ordered Mott insulator, and (b) in a paramagnetic state, both based on $MoSe_2/WSe_2$. $Q_x$ and $Q_y$ denote components of the exciton momentum, with the moiré Brillouin zone shown as a hexagon. High-symmetry points $\Gamma$, $\kappa$, and $M$ are indicated. (c) Comparison of excitonic bandwidths from a magnetically ordered background ($W_X^{MO}$) and a paramagnetic background ($W_X^{PM}$) as functions of moiré period. Figure reproduced from Ref. [3].

ments in doped moiré bilayers [6]. Intuitively, this is because the diffusion constant of a quasiparticle is inversely related to its effective mass, which is approximately captured by the inverse of its bandwidth. To probe and distinguish the exciton dynamics in antiferromagnetically correlated and paramagnetic backgrounds, at least two sets of measurements — conducted at temperatures much lower and much higher than $J$, respectively — are required. The results above predict that the former case will exhibit a significantly smaller diffusion constant compared to the latter.

# Chapter 6: Conclusion and outlook

## 6.1 Summary

We have reviewed the theoretical descriptions of three distinct classes of strongly correlated moiré excitons. To reiterate, in Section 3, we discussed a scenario in which single-exciton dynamics are constrained by charge ordering of doped electrons due to exciton-electron repulsion. As a result, the optical and topological properties of the exciton depend on the geometric structure of the charge order, which can be tuned via gate voltages. Notably, because moiré TMDs lie in the deep subwavelength regime, excitonic emission exhibits an order-of-magnitude collective enhancement. In Section 4, we discussed situations involving multiple moiré excitons and the impact of their nonbosonic character, which is generally non-negligible in these bilayer systems. This statistical property manifests as a phase space filling effect between composite particles, imposing an upper bound on the number of excitons per moiré unit cell. Consequently, excitonic behavior deviates from that predicted by the conventional Bose-Hubbard model when the system is optically driven at high powers. Finally, in Section 5, we reviewed a framework for describing an exciton embedded in a frustrated spin-ordered Mott insulator. Such a bound state becomes dressed by the underlying magnetic fluctuations, leading to a substantial suppression of its effective tunneling compared to a similar excitonic species in a paramagnetic background.

These excitonic species can potentially be probed through the following respective experimental approaches. First, the collective excitonic properties discussed in Section 3 can be extracted via far-field reflection measurements. In particular, when combined with momentum resolution controlled by the incident angle and polarization resolution, the Berry curvatures of excitonic bands can be inferred from the scattering matrix. Such measurements could be employed to probe and distinguish charge-ordered states with different geometric structures. Next, the nonbosonic nature of moiré excitons discussed in Section 4 may manifest in photoluminescence experiments conducted at high pump power. The corresponding emission spectrum is predicted to exhibit a series of lines that are equally spaced in frequency below a critical power threshold, which reveals the filling bound imposed by nonbosonicity. Above this threshold, the spectral lines generally lose the equal-spacing feature due to the involvement of higher excitonic orbitals. Finally, the magnetically dressed Mott exciton described in Section 5 may be identified through low-temperature exciton diffusion measurements in doped bilayers with integer charge filling. Its diffusion constant is expected to be significantly smaller than that of an exciton in a paramagnetic background, which can be accessed in a similar measurement at higher temperatures.

## 6.2 Outlooks

In addition to the works discussed above, excitons and electrons in moiré TMDs provide a rich platform for exploring a wide range of electron-photon physics and quantum optics phenomena. Below, we outline several such directions, beginning with the potential interplay between a single moiré exciton and electronic states, and concluding with prospects

for many-exciton systems.

The idea of probing charge and spin orders using a single exciton can be generalized to other correlated electronic states that emerge in moiré TMDs. These states include Kondo insulators [31, 32, 33], superconductors [34, 35, 36, 37, 38, 39], and topological phases such as (fractional) Chern insulators [40, 41, 42, 43, 44]. Experimental efforts to probe these states have primarily focused on transport techniques. Although optical probes have been implemented, they typically provide only indirect signatures — for example, magnetic circular dichroism to identify ferromagnetic correlations — which only serve as complementary evidence supporting transport measurements. As a result, direct optical signatures of these correlated electronic states remain elusive, and the theoretical understanding of exciton-electron coupling in such systems remains an open problem.

Besides the excitonic physics in doped bilayers, optical emitters in undoped bilayers can also exhibit a variety of intriguing many-body phenomena. For instance, in the many-exciton regime, the collective interference effect discussed in Section 3 could potentially give rise to a superradiant burst — a phenomenon that has attracted significant interest in the quantum optics community. Another example is the impact of nonbosonicity on the many-body phase diagram of excitons, which has previously been described by the standard Bose-Hubbard model. How the superfluid–Mott insulator transition is modified by the phase space filling effect remains a widely open question.

These moiré excitons may even be harnessed to simulate the physics of topological quantum many-body optics. This possibility is supported by the presence of nontrivial Berry curvatures arising from collective interference effects, as well as the narrow excitonic bandwidths relative to exciton-exciton interaction energies. A prominent phenomenon in

this category is the (fractional) quantum Hall effect of excitons (distinct from the electronic counterpart discussed earlier). Other intriguing effects, such as the emergence of non-Abelian anyons, may also arise due to the effective high-order interactions induced by excitonic nonbosonicity, as discussed in Section 4. With these promising directions, we anticipate that moiré excitons will significantly broaden the scope of many-body quantum optics.

# Bibliography


[1] Tsung-Sheng Huang, Yu-Xin Wang, Yan-Qi Wang, Darrick Chang, Mohammad Hafezi, and Andrey Grankin. Collective optical properties of moir\'e excitons. *arXiv preprint arXiv:2407.19611*, 2024.

[2] Tsung-Sheng Huang, Peter Lunts, and Mohammad Hafezi. Nonbosonic moiré excitons. *Physical Review Letters*, 132(18):186202, 2024.

[3] Tsung-Sheng Huang, Yang-Zhi Chou, Christopher L Baldwin, Fengcheng Wu, and Mohammad Hafezi. Mott-moiré excitons. *Physical Review B*, 107(19):195151, 2023.

[4] T-S Huang, CL Baldwin, M Hafezi, and V Galitski. Spin-mediated mott excitons. *Physical Review B*, 107(7):075111, 2023.

[5] Beini Gao, Daniel G Suárez-Forero, Supratik Sarkar, Tsung-Sheng Huang, Deric Session, Mahmoud Jalali Mehrabad, Ruihao Ni, Ming Xie, Pranshoo Upadhyay, Jonathan Vannucci, et al. Excitonic mott insulator in a bose-fermi-hubbard system of moiré ws2/wse2 heterobilayer. *Nature Communications*, 15(1):2305, 2024.

[6] Pranshoo Upadhyay, Daniel G Suárez-Forero, Tsung-Sheng Huang, Mahmoud Jalali Mehrabad, Beini Gao, Supratik Sarkar, Deric Session, Kenji Watanabe, Takashi Taniguchi, You Zhou, et al. Giant enhancement of exciton diffusion near an electronic mott insulator. *arXiv preprint arXiv:2409.18357*, 2024.

[7] Jacqueline Bloch, Andrea Cavalleri, Victor Galitski, Mohammad Hafezi, and Angel Rubio. Strongly correlated electron–photon systems. *Nature*, 606(7912):41–48, 2022.

[8] Dimitri N Basov, Richard D Averitt, Dirk Van Der Marel, Martin Dressel, and Kristjan Haule. Electrodynamics of correlated electron materials. *Reviews of Modern Physics*, 83(2):471–541, 2011.

[9] Iacopo Carusotto and Cristiano Ciuti. Quantum fluids of light. *Reviews of Modern Physics*, 85(1):299–366, 2013.

[10] Frank Schlawin, Dante M Kennes, and Michael A Sentef. Cavity quantum materials. *Applied Physics Reviews*, 9(1), 2022.

[11] Jonathan A Sobota, Yu He, and Zhi-Xun Shen. Angle-resolved photoemission studies of quantum materials. *Reviews of Modern Physics*, 93(2):025006, 2021.

[12] Tobia F Nova, Andrea Cartella, Alice Cantaluppi, Michael Först, Davide Bossini, Rostislav V Mikhaylovskiy, Aleksei V Kimel, Roberto Merlin, and Andrea Cavalleri. An effective magnetic field from optically driven phonons. *Nature Physics*, 13(2):132–136, 2017.

[13] Ankit S Disa, Michael Fechner, Tobia F Nova, Biaolong Liu, Michael Först, Dharmalingam Prabhakaran, Paolo G Radaelli, and Andrea Cavalleri. Polarizing an antiferromagnet by optical engineering of the crystal field. *Nature Physics*, 16(9):937–941, 2020.

[14] Daniele Fausti, RI Tobey, Nicky Dean, Stefan Kaiser, A Dienst, Matthias C Hoffmann, S Pyon, T Takayama, H Takagi, and Andrea Cavalleri. Light-induced superconductivity in a stripe-ordered cuprate. *science*, 331(6014):189–191, 2011.

[15] Matteo Mitrano, Alice Cantaluppi, Daniele Nicoletti, Stefan Kaiser, A Perucchi, Stefano Lupi, P Di Pietro, Daniele Pontiroli, Mauro Riccò, Stephen R Clark, et al. Possible light-induced superconductivity in k3c60 at high temperature. *Nature*, 530(7591):461–464, 2016.

[16] Chia-Jung Yang, Jingwen Li, Manfred Fiebig, and Shovon Pal. Terahertz control of many-body dynamics in quantum materials. *Nature Reviews Materials*, 8(8):518–532, 2023.

[17] Xinge Yu, Tobin J Marks, and Antonio Facchetti. Metal oxides for optoelectronic applications. *Nature materials*, 15(4):383–396, 2016.

[18] Lei Zhang, Yuanjun Zhou, Lu Guo, Weiwei Zhao, Anna Barnes, Hai-Tian Zhang, Craig Eaton, Yuanxia Zheng, Matthew Brahlek, Hamna F Haneef, et al. Correlated metals as transparent conductors. *Nature materials*, 15(2):204–210, 2016.

[19] Mikko Turunen, Mauro Brotons-Gisbert, Yunyun Dai, Yadong Wang, Eleanor Scerri, Cristian Bonato, Klaus D Jöns, Zhipei Sun, and Brian D Gerardot. Quantum photonics with layered 2d materials. *Nature Reviews Physics*, 4(4):219–236, 2022.

[20] Dante M Kennes, Martin Claassen, Lede Xian, Antoine Georges, Andrew J Millis, James Hone, Cory R Dean, DN Basov, Abhay N Pasupathy, and Angel Rubio. Moiré heterostructures as a condensed-matter quantum simulator. *Nature Physics*, 17(2):155–163, 2021.

[21] Nathan P Wilson, Wang Yao, Jie Shan, and Xiaodong Xu. Excitons and emergent quantum phenomena in stacked 2d semiconductors. *Nature*, 599(7885):383–392, 2021.

[22] Kin Fai Mak and Jie Shan. Semiconductor moiré materials. *Nature Nanotechnology*, 17(7):686–695, 2022.

[23] Luojun Du, Maciej R Molas, Zhiheng Huang, Guangyu Zhang, Feng Wang, and Zhipei Sun. Moiré photonics and optoelectronics. *Science*, 379(6639):eadg0014, 2023.

[24] Jun Kang, Sefaattin Tongay, Jian Zhou, Jingbo Li, and Junqiao Wu. Band offsets and heterostructures of two-dimensional semiconductors. *Applied Physics Letters*, 102(1), 2013.

[25] Pasqual Rivera, Hongyi Yu, Kyle L Seyler, Nathan P Wilson, Wang Yao, and Xiaodong Xu. Interlayer valley excitons in heterobilayers of transition metal dichalcogenides. *Nature nanotechnology*, 13(11):1004–1015, 2018.

[26] Fengcheng Wu, Timothy Lovorn, Emanuel Tutuc, and Allan H MacDonald. Hubbard model physics in transition metal dichalcogenide moiré bands. *Physical review letters*, 121(2):026402, 2018.

[27] Tomasz Smoleński, Pavel E Dolgirev, Clemens Kuhlenkamp, Alexander Popert, Yuya Shimazaki, Patrick Back, Xiaobo Lu, Martin Kroner, Kenji Watanabe, Takashi Taniguchi, et al. Signatures of wigner crystal of electrons in a monolayer semiconductor. *Nature*, 595(7865):53–57, 2021.

[28] Haining Pan, Fengcheng Wu, and Sankar Das Sarma. Quantum phase diagram of a moiré-hubbard model. *Physical Review B*, 102(20):201104, 2020.

[29] Yang Xu, Song Liu, Daniel A Rhodes, Kenji Watanabe, Takashi Taniguchi, James Hone, Veit Elser, Kin Fai Mak, and Jie Shan. Correlated insulating states at fractional fillings of moiré superlattices. *Nature*, 587(7833):214–218, 2020.

[30] Yanhao Tang, Lizhong Li, Tingxin Li, Yang Xu, Song Liu, Katayun Barmak, Kenji Watanabe, Takashi Taniguchi, Allan H MacDonald, Jie Shan, et al. Simulation of hubbard model physics in wse2/ws2 moiré superlattices. *Nature*, 579(7799):353–358, 2020.

[31] Ajesh Kumar, Nai Chao Hu, Allan H MacDonald, and Andrew C Potter. Gate-tunable heavy fermion quantum criticality in a moiré kondo lattice. *Physical Review B*, 106(4):L041116, 2022.

[32] Daniele Guerci, Jie Wang, Jiawei Zang, Jennifer Cano, JH Pixley, and Andrew Millis. Chiral kondo lattice in doped mote2/wse2 bilayers. *Science Advances*, 9(11):eade7701, 2023.

[33] Wenjin Zhao, Bowen Shen, Zui Tao, Zhongdong Han, Kaifei Kang, Kenji Watanabe, Takashi Taniguchi, Kin Fai Mak, and Jie Shan. Gate-tunable heavy fermions in a moiré kondo lattice. *Nature*, 616(7955):61–65, 2023.

[34] Hongli Guo, Xu Zhang, and Gang Lu. Shedding light on moiré excitons: A first-principles perspective. *Science advances*, 6(42):eabc5638, 2020.

[35] Yiyu Xia, Zhongdong Han, Kenji Watanabe, Takashi Taniguchi, Jie Shan, and Kin Fai Mak. Superconductivity in twisted bilayer wse2. *Nature*, pages 1–6, 2024.

[36] Chuyi Tuo, Ming-Rui Li, Zhengzhi Wu, Wen Sun, and Hong Yao. Theory of topological superconductivity and antiferromagnetic correlated insulators in twisted bilayer wse2. *arXiv preprint arXiv:2409.06779*, 2024.

[37] Jihang Zhu, Yang-Zhi Chou, Ming Xie, and Sankar Das Sarma. Superconductivity in twisted transition metal dichalcogenide homobilayers. *arXiv preprint arXiv:2406.19348*, 2024.

[38] Yinjie Guo, Jordan Pack, Joshua Swann, Luke Holtzman, Matthew Cothrine, Kenji Watanabe, Takashi Taniguchi, David G Mandrus, Katayun Barmak, James Hone, et al. Superconductivity in 5.0° twisted bilayer wse2. *Nature*, 637(8047):839–845, 2025.

[39] Sunghoon Kim, Juan Felipe Mendez-Valderrama, Xuepeng Wang, and Debanjan Chowdhury. Theory of correlated insulators and superconductor at $\nu = 1$ in twisted wse2. *Nature Communications*, 16(1):1701, 2025.

[40] Jiaqi Cai, Eric Anderson, Chong Wang, Xiaowei Zhang, Xiaoyu Liu, William Holtzmann, Yinong Zhang, Fengren Fan, Takashi Taniguchi, Kenji Watanabe, et al. Signatures of fractional quantum anomalous hall states in twisted mote2. *Nature*, 622(7981):63–68, 2023.

[41] Heonjoon Park, Jiaqi Cai, Eric Anderson, Yinong Zhang, Jiayi Zhu, Xiaoyu Liu, Chong Wang, William Holtzmann, Chaowei Hu, Zhaoyu Liu, et al. Observation of fractionally quantized anomalous hall effect. *Nature*, 622(7981):74–79, 2023.

[42] Yihang Zeng, Zhengchao Xia, Kaifei Kang, Jiacheng Zhu, Patrick Knüppel, Chirag Vaswani, Kenji Watanabe, Takashi Taniguchi, Kin Fai Mak, and Jie Shan. Thermodynamic evidence of fractional chern insulator in moiré mote2. *Nature*, 622(7981):69–73, 2023.

[43] Kaifei Kang, Bowen Shen, Yichen Qiu, Yihang Zeng, Zhengchao Xia, Kenji Watanabe, Takashi Taniguchi, Jie Shan, and Kin Fai Mak. Evidence of the fractional quantum spin hall effect in moiré mote2. *Nature*, 628(8008):522–526, 2024.

[44] Chong Wang, Xiao-Wei Zhang, Xiaoyu Liu, Yuchi He, Xiaodong Xu, Ying Ran, Ting Cao, and Di Xiao. Fractional chern insulator in twisted bilayer mote 2. *Physical Review Letters*, 132(3):036501, 2024.

[45] H. Haug and S. W. Koch. *Quantum Theory of the Optical and Electronic Properties of Semiconductors*. World Scientific, 2004.

[46] Shengnan Miao, Tianmeng Wang, Xiong Huang, Dongxue Chen, Zhen Lian, Chong Wang, Mark Blei, Takashi Taniguchi, Kenji Watanabe, Sefaattin Tongay, et al. Strong interaction between interlayer excitons and correlated electrons in wse2/ws2 moiré superlattice. *Nature communications*, 12(1):3608, 2021.

[47] Richen Xiong, Jacob H Nie, Samuel L Brantly, Patrick Hays, Renee Sailus, Kenji Watanabe, Takashi Taniguchi, Sefaattin Tongay, and Chenhao Jin. Correlated insulator of excitons in wse2/ws2 moiré superlattices. *Science*, 380(6647):860–864, 2023.

[48] Qinghai Tan, Abdullah Rasmita, Zhaowei Zhang, Hongbing Cai, Xiangbin Cai, Xuran Dai, Kenji Watanabe, Takashi Taniguchi, Allan H MacDonald, and Weibo Gao. Layer-dependent correlated phases in wse2/mos2 moiré superlattice. *Nature Materials*, 22(5):605–611, 2023.

[49] Livio Ciorciaro, T Smoleński, Ivan Morera, Natasha Kiper, Sarah Hiestand, Martin Kroner, Yang Zhang, Kenji Watanabe, Takashi Taniguchi, Eugene Demler, et al. Kinetic magnetism in triangular moiré materials. *Nature*, 623(7987):509–513, 2023.

[50] JR Leonard, Lunhui Hu, AA High, AT Hammack, Congjun Wu, LV Butov, KL Campman, and AC Gossard. Moiré pattern of interference dislocations in condensate of indirect excitons. *Nature communications*, 12(1):1175, 2021.

[51] Jacob Cutshall, Fateme Mahdikhany, Anna Roche, Daniel N Shanks, Michael R Koehler, David G Mandrus, Takashi Taniguchi, Kenji Watanabe, Qizhong Zhu, Brian J LeRoy, et al. Imaging interlayer exciton superfluidity in a 2d semiconductor heterostructure. *Science Advances*, 11(1):eadr1772, 2025.

[52] Alexey Kavokin, Guillaume Malpuech, and Fabrice P Laussy. Polariton laser and polariton superfluidity in microcavities. *Physics Letters A*, 306(4):187–199, 2003.

[53] Heonjoon Park, Jiayi Zhu, Xi Wang, Yingqi Wang, William Holtzmann, Takashi Taniguchi, Kenji Watanabe, Jiaqiang Yan, Liang Fu, Ting Cao, et al. Dipole ladders with large hubbard interaction in a moiré exciton lattice. *Nature Physics*, 19(9):1286–1292, 2023.

[54] Amine Ben Mhenni, Wilhelm Kadow, Mikołaj J Metelski, Adrian O Paulus, Alain Dijkstra, Kenji Watanabe, Takashi Taniguchi, Seth Ariel Tongay, Matteo Barbone, Jonathan J Finley, et al. Gate-tunable bose-fermi mixture in a strongly correlated moir\'e bilayer electron system. *arXiv preprint arXiv:2410.07308*, 2024.

[55] Di Xiao, Gui-Bin Liu, Wanxiang Feng, Xiaodong Xu, and Wang Yao. Coupled spin and valley physics in monolayers of mos 2 and other group-vi dichalcogenides. *Physical review letters*, 108(19):196802, 2012.

[56] Gui-Bin Liu, Wen-Yu Shan, Yugui Yao, Wang Yao, and Di Xiao. Three-band tight-binding model for monolayers of group-vib transition metal dichalcogenides. *Physical Review B—Condensed Matter and Materials Physics*, 88(8):085433, 2013.

[57] Kha Tran, Galan Moody, Fengcheng Wu, Xiaobo Lu, Junho Choi, Kyounghwan Kim, Amritesh Rai, Daniel A Sanchez, Jiamin Quan, Akshay Singh, et al. Evidence for moiré excitons in van der waals heterostructures. *Nature*, 567(7746):71–75, 2019.

[58] Fengcheng Wu, Timothy Lovorn, Emanuel Tutuc, Ivar Martin, and AH MacDonald. Topological insulators in twisted transition metal dichalcogenide homobilayers. *Physical review letters*, 122(8):086402, 2019.

[59] Hongyuan Li, Shaowei Li, Mit H Naik, Jingxu Xie, Xinyu Li, Emma Regan, Danqing Wang, Wenyu Zhao, Kentaro Yumigeta, Mark Blei, et al. Imaging local discharge cascades for correlated electrons in ws2/wse2 moiré superlattices. *Nature Physics*, 17(10):1114–1119, 2021.

[60] Hongyuan Li, Shaowei Li, Mit H Naik, Jingxu Xie, Xinyu Li, Jiayin Wang, Emma Regan, Danqing Wang, Wenyu Zhao, Sihan Zhao, et al. Imaging moiré flat bands in three-dimensional reconstructed wse2/ws2 superlattices. *Nature materials*, 20(7):945–950, 2021.

[61] Ya-Hui Zhang, DN Sheng, and Ashvin Vishwanath. Su (4) chiral spin liquid, exciton supersolid, and electric detection in moiré bilayers. *Physical review letters*, 127(24):247701, 2021.

[62] Mit H Naik, Emma C Regan, Zuocheng Zhang, Yang-Hao Chan, Zhenglu Li, Danqing Wang, Yoseob Yoon, Chin Shen Ong, Wenyu Zhao, Sihan Zhao, et al. Intralayer charge-transfer moiré excitons in van der waals superlattices. *Nature*, 609(7925):52–57, 2022.

[63] Evgeny M Alexeev, David A Ruiz-Tijerina, Mark Danovich, Matthew J Hamer, Daniel J Terry, Pramoda K Nayak, Seongjoon Ahn, Sangyeon Pak, Juwon Lee, Jung Inn Sohn, et al. Resonantly hybridized excitons in moiré superlattices in van der waals heterostructures. *Nature*, 567(7746):81–86, 2019.

[64] Niclas Götting, Frederik Lohof, and Christopher Gies. Moiré-bose-hubbard model for interlayer excitons in twisted transition metal dichalcogenide heterostructures. *Physical Review B*, 105(16):165419, 2022.

[65] Hongyi Yu, Gui-Bin Liu, Jianju Tang, Xiaodong Xu, and Wang Yao. Moiré excitons: From programmable quantum emitter arrays to spin-orbit–coupled artificial lattices. *Science advances*, 3(11):e1701696, 2017.

[66] Fengcheng Wu, Timothy Lovorn, and AH MacDonald. Theory of optical absorption by interlayer excitons in transition metal dichalcogenide heterobilayers. *Physical Review B*, 97(3):035306, 2018.

[67] Elyse Barré, Ouri Karni, Erfu Liu, Aidan L O'Beirne, Xueqi Chen, Henrique B Ribeiro, Leo Yu, Bumho Kim, Kenji Watanabe, Takashi Taniguchi, et al. Optical absorption of interlayer excitons in transition-metal dichalcogenide heterostructures. *Science*, 376(6591):406–410, 2022.

[68] Yong Wang, Zhan Wang, Wang Yao, Gui-Bin Liu, and Hongyi Yu. Interlayer coupling in commensurate and incommensurate bilayer structures of transition-metal dichalcogenides. *Physical Review B*, 95(11):115429, 2017.

[69] Kyle L Seyler, Pasqual Rivera, Hongyi Yu, Nathan P Wilson, Essance L Ray, David G Mandrus, Jiaqiang Yan, Wang Yao, and Xiaodong Xu. Signatures of moiré-trapped valley excitons in mose2/wse2 heterobilayers. *Nature*, 567(7746):66–70, 2019.

[70] Xiong Huang, Tianmeng Wang, Shengnan Miao, Chong Wang, Zhipeng Li, Zhen Lian, Takashi Taniguchi, Kenji Watanabe, Satoshi Okamoto, Di Xiao, et al. Correlated insulating states at fractional fillings of the ws2/wse2 moiré lattice. *Nature Physics*, 17(6):715–719, 2021.

[71] Ming Xie, Mohammad Hafezi, and Sankar Das Sarma. Long-lived topological flat-band excitons in semiconductor moir\'e heterostructures: a bosonic kane-mele model platform. *arXiv preprint arXiv:2403.00052*, 2024.

[72] Arturo Camacho-Guardian and Nigel R Cooper. Moiré-induced optical nonlinearities: single-and multiphoton resonances. *Physical Review Letters*, 128(20):207401, 2022.

[73] Benjamin Remez and Nigel R Cooper. Leaky exciton condensates in transition metal dichalcogenide moiré bilayers. *Physical Review Research*, 4(2):L022042, 2022.

[74] Hartmut Haug and Stefan Schmitt-Rink. Electron theory of the optical properties of laser-excited semiconductors. *Progress in Quantum Electronics*, 9(1):3–100, 1984.

[75] Monique Combescot, Odile Betbeder-Matibet, and François Dubin. The many-body physics of composite bosons. *Physics Reports*, 463(5-6):215–320, 2008.

[76] Assa Auerbach. *Interacting electrons and quantum magnetism*. Springer Science & Business Media, 2012.

[77] Ouri Karni, Elyse Barré, Vivek Pareek, Johnathan D Georgaras, Michael KL Man, Chakradhar Sahoo, David R Bacon, Xing Zhu, Henrique B Ribeiro, Aidan L O'Beirne, et al. Structure of the moiré exciton captured by imaging its electron and hole. *Nature*, 603(7900):247–252, 2022.

[78] Mohamed Azzouz and Thierry Dombre. Motion of holes on the triangular lattice studied using the t-j model. *Physical Review B*, 53(1):402, 1996.

[79] Shuai A Chen, Qianqian Chen, and Zheng Zhu. Proposal for asymmetric photoemission and tunneling spectroscopies in quantum simulators of the triangular-lattice fermi-hubbard model. *Physical Review B*, 106(8):085138, 2022.

[80] Gerardo Martinez and Peter Horsch. Spin polarons in the t-j model. *Physical Review B*, 44(1):317, 1991.

[81] Matthias Vojta. Spin polarons in triangular antiferromagnets. *Physical Review B*, 59(9):6027, 1999.

[82] Fabian Grusdt, Marton Kanasz-Nagy, Annabelle Bohrdt, Christie S Chiu, Geoffrey Ji, Markus Greiner, Daniel Greif, and Eugene Demler. Parton theory of magnetic polarons: Mesonic resonances and signatures in dynamics. *Physical Review X*, 8(1):011046, 2018.

[83] J Fröhlich and PA Marchetti. Slave fermions, slave bosons, and semions from bosonization of the two-dimensional t-j model. *Physical Review B*, 46(10):6535, 1992.

[84] Shiping Feng, ZB Su, and Lu Yu. Fermion-spin transformation to implement the charge-spin separation. *Physical Review B*, 49(4):2368, 1994.

[85] Akihiro Shimizu, Koji Aoki, Kazuhiko Sakakibara, Ikuo Ichinose, and Tetsuo Matsui. Antiferromagnetic, metal-insulator, and superconducting phase transitions in underdoped cuprates: Slave-fermion t-j model in the hopping expansion. *Physical Review B—Condensed Matter and Materials Physics*, 83(6):064502, 2011.

[86] Xing-Jie Han, Yu Liu, Zhi-Yuan Liu, Xin Li, Jing Chen, Hai-Jun Liao, Zhi-Yuan Xie, B Normand, and Tao Xiang. Charge dynamics of the antiferromagnetically ordered mott insulator. *New Journal of Physics*, 18(10):103004, 2016.

[87] Nick Bultinck, Eslam Khalaf, Shang Liu, Shubhayu Chatterjee, Ashvin Vishwanath, and Michael P Zaletel. Ground state and hidden symmetry of magic-angle graphene at even integer filling. *Physical Review X*, 10(3):031034, 2020.

[88] Andrey V Chubukov and Steven A Kivelson. Superconductivity in engineered two-dimensional electron gases. *Physical Review B*, 96(17):174514, 2017.